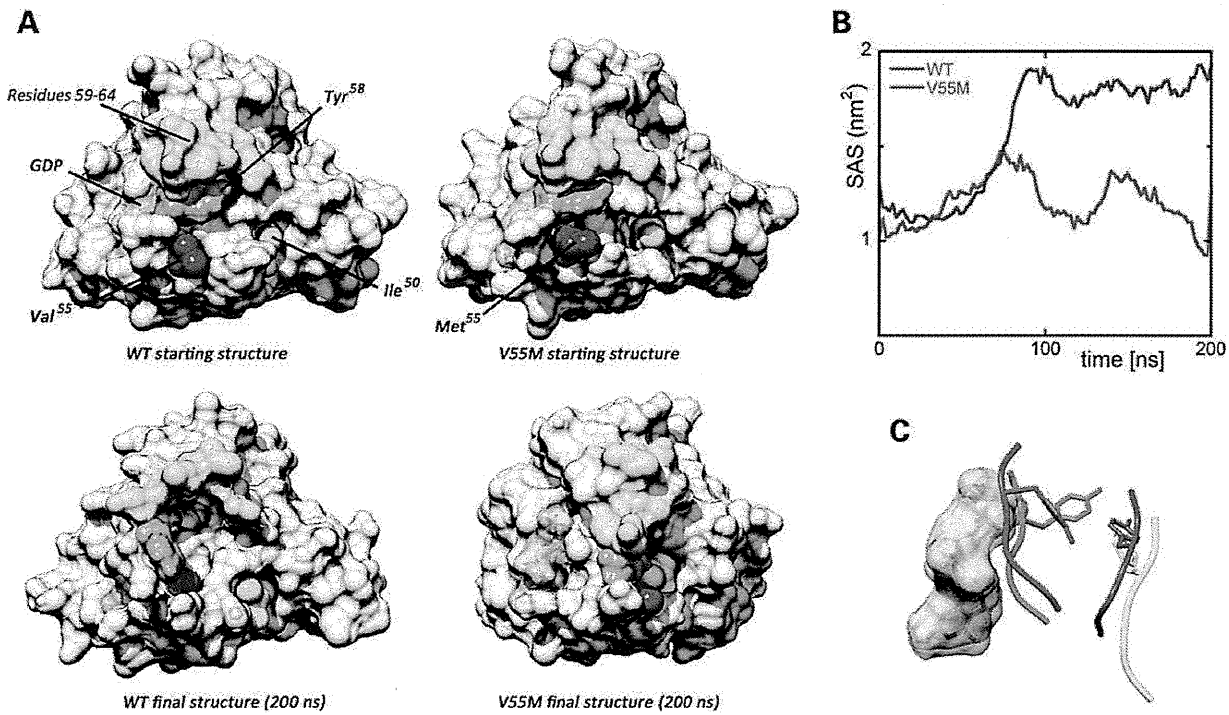

Figure 2. Molecular dynamics (MD) simulations. (**A**) Structural perturbations promoted by the p.Val55Met substitution as obtained from MD simulations of the RRAS/GDP complex. The wild-type (WT) protein is also shown for comparison. Top panels report the protein structures at the beginning of simulations, whereas the final structures (200 ns) are shown at the bottom. The final structure of $RRAS^{V55M}$ is well representative of the last 120 ns of the trajectory. The protein surface of RRAS is shown with GDP (yellow). The mutated residues and those forming a cluster in the simulation of mutated RRAS are coloured as follows: Val^{55}/Met^{55} (blue), Tyr^{58} (pink) and Ile^{50} (cyan). Residues 59–64, which, together with Tyr^{58}, form the switch I region, are coloured in green. (**B**) Solvent accessible surface of GDP in the MD simulations of wild-type (red) and mutant (blue) RRAS/GDP complexes. (**C**) Conformation of the loop comprised between Val^{55}/Met^{55} and Asp^{59} in wild-type (red) and mutant (blue) RRAS/GDP complexes obtained from MD simulations. GDP is reported as semi-transparent yellow surface. Superimposed conformations of the corresponding loop (residues 29–33) in GDP-bound HRAS (violet) (PDB: 4Q21) and GDP-bound HRAS complexed with SOS1 (cyan) (PDB: 1BKD) are shown for comparison. The side chains of Tyr^{58} and the corresponding residue in HRAS, Tyr^{32}, are displayed as sticks.

and extent of signalling through the MAPK and PI3K/AKT cascades were evaluated using transient expression in COS-7 cells. Consistent with the above-mentioned findings, pull-down assays revealed a variably higher proportion of active, GTP-bound form for both mutants (Fig. 4A). Moreover, similarly to what observed under cell-free conditions, $RRAS^{G39dup}$ was resistant to GAP stimulation. Expression of both mutants promoted enhanced serum-dependent MEK, ERK and AKT phosphorylation (Fig. 4B), which was more evident in cells expressing the $RRAS^{G39dup}$ mutant.

Caenorhabditis elegans studies

To explore further the functional impact of the RASopathy causative RRAS mutants on RAS signalling *in vivo*, we used the nematode *C. elegans* as an experimental model. In *C. elegans*, the role of *ras-1*, the *RRAS* ortholog (33), has not been characterized yet. On the contrary, proper signalling through LET-60, the *C. elegans* ortholog of RAS proteins, has been established to play a crucial role in vulval development (34). In particular, LET-60/RAS is known to mediate the priming signal (LIN-3/EGF) released by the anchor cell to induce the three nearby vulval precursor cells (VPCs), P5.p, P6.p and P7.p, to generate a normal vulva. Enhanced and decreased signalling through LET-60 and the MAPK cassette results in multiple ectopic pseudovulvae (multivulva phenotype) and a failure in VPC induction (vulvaless phenotype), respectively (34,35).

Multiple transgenic lines were generated to conditionally express the wild-type *ras-1* cDNA ($ras\text{-}1^{WT}$) or the allele homologous to the disease-associated three-nucleotide duplication ($ras\text{-}1^{G27dup}$), which was identified to occur both as a germline and somatic event. Exogenous RAS-1 expression was induced by heat shock at early L3 larval stage to investigate the effects of the mutant protein on vulval development. Animals expressing $ras\text{-}1^{G27dup}$ displayed abnormal vulval morphogenesis resulting in the formation of a protruding vulva (Pvl) (Fig. 5A and B and Supplementary Material, Table S6), a phenotype associated with aberrant traffic through different signalling cascades (36,37). Of note, this phenotype had previously been reported in worms expressing the RASopathy causative $SHOC2^{S2G}$ mutant (38). Like those animals, $ras\text{-}1^{G27dup}$ worms showed decreased egg-laying efficiency (Egl phenotype), and accumulation of larvae inside the mother (Bag-of-worms phenotype). A significantly less penetrant phenotype was observed in animals expressing $ras\text{-}1^{WT}$. These findings, together with the observation that animals lacking *ras-1* do not exhibit any vulval defect (WormBase, http://www.wormbase.org/, and our personal assessment), supported the gain-of-function role of the mutation on RAS-1 function. At the late L3/early L4 larval stage, vulva

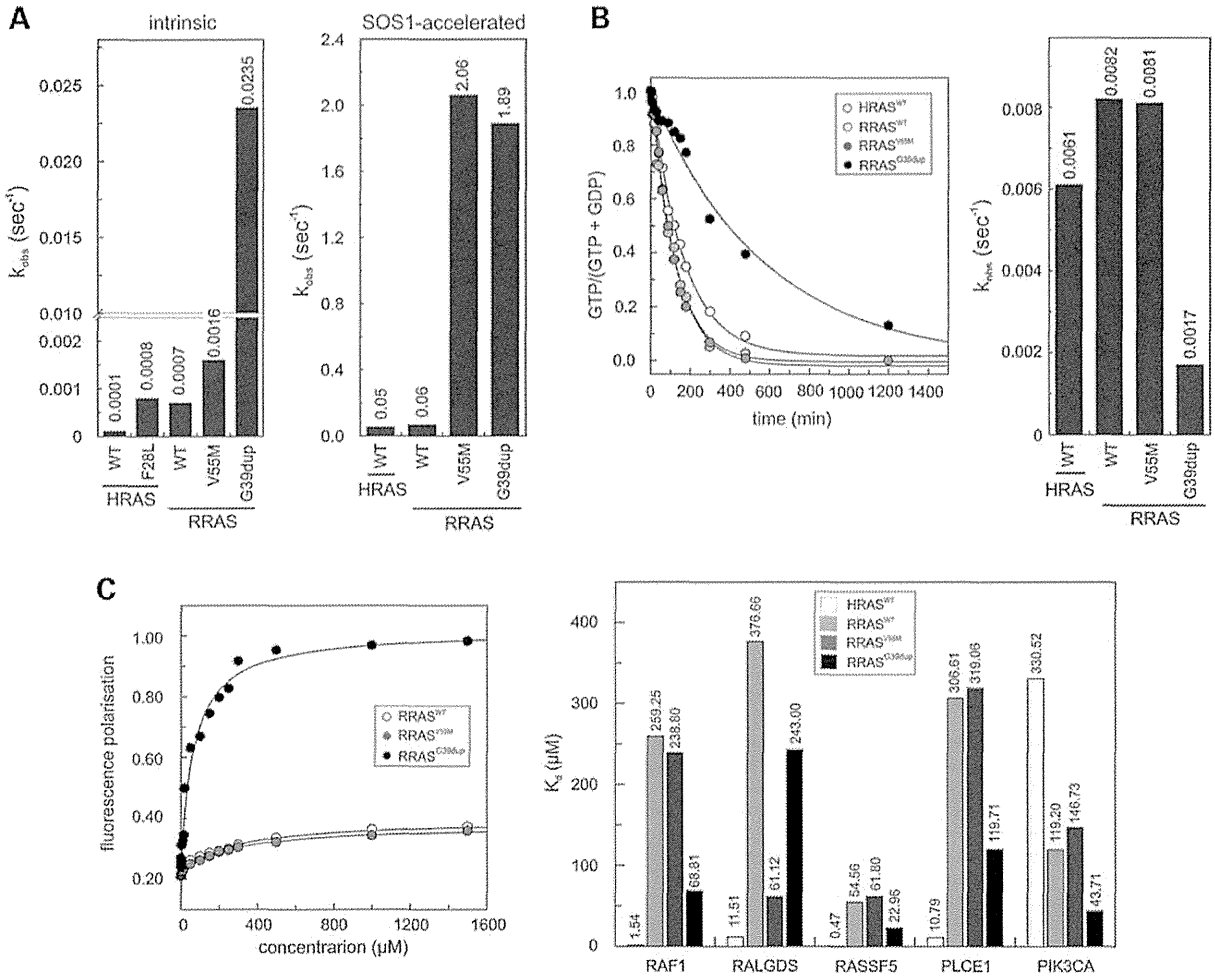

Figure 3. *In vitro* biochemical characterization of the RRAS^{G39dup} and RRAS^{V55M} mutants. (**A**) Intrinsic (left) and SOS1-accelerated (right) mantGDP nucleotide dissociation measured in the presence of 20-fold excess of non-labelled GDP. The decrease in mant fluorescence was fitted by single exponentials to obtain k_{obs} values for nucleotide dissociation. RRAS^{G39dup} exhibited a 35-fold increased intrinsic dissociation of mantGDP, whereas SOS1-accelerated mantGDP dissociation was augmented by ~30-fold for both mutants, compared with RRAS^{WT} and HRAS^{WT}. The K_{obs} values are an average of five to seven independent measurements. (**B**) Intrinsic GTP hydrolysis kinetics (left) and rate constants (right) of RRAS^{G39dup} and RRAS^{V55M} proteins, documenting the impaired catalytic activity in the former. The K_{obs} values are an average of five to seven independent measurements. (**C**) Binding of RRAS^{WT}, RRAS^{V55M} and RRAS^{G39dup} to the RAS-binding domain of RAF1 measured as variation in fluorescence polarization of each mantGppNHp-bound RRAS protein at increasing concentrations of RAF1-RBD (left), and dissociation constants (K_d) for the interaction of HRAS^{WT} and RRAS proteins to the RBDs of RAF1, RALGDS, PLCE1, PIK3CA and RASSF5 (right). K_d values were obtained by quadratic fitting of the concentration-dependent binding curves from fluorescence polarization measurement as exemplified for RAF1-RBD. Of note, RRAS^{WT} binds to RAF1, RALGDS, RASSF5 and PLCE1 less efficiently than HRAS, whereas an increased binding affinity to PIK3CA is observed.

morphogenesis normally begins with the descendants of VPC P6.p detaching from the cuticle and forming a symmetric invagination (Fig. 5C) (34). Animals in which the expression of *ras-1*^{WT} had been induced at early L3 largely maintained this pattern (17/20). In contrast, in larvae expressing *ras-1*^{G27dup}, descendants of VPCs P5.p and/or P7.p more frequently detached from the cuticle, resulting in larger and more asymmetric invaginations (10/30). This morphogenesis defect was the earliest detectable effect of the *ras-1*^{G27dup} allele on vulval development, similarly to that previously documented in transgenic lines expressing SHOC2^{S2G} (38).

Genetic interaction between the RAS-1/RRAS mutant and LET-60/RAS was also investigated. While expression of the RAS-1^{G27dup} mutant was able to exacerbate the multivulva phenotype associated with a hyperactive *let-60* allele (*n1046*), expression of wild-type RAS-1 failed to do so (Table 1). Similarly, a significant, although partial rescue of the VPC induction defect associated with a *let-23/EGFR* hypomorphic allele (*sy1*) was observed in animals expressing the activating RAS-1^{G27dup} mutant, but not in worms expressing the wild-type counterpart (Table 1). Overall, these experiments provided evidence of a positive modulatory role of the RAS-1/RRAS mutant on LET-60/RAS signalling.

DISCUSSION

Mutations of genes coding for proteins with role in RAS signalling and the RAF/MEK/ERK cascade have been identified as the

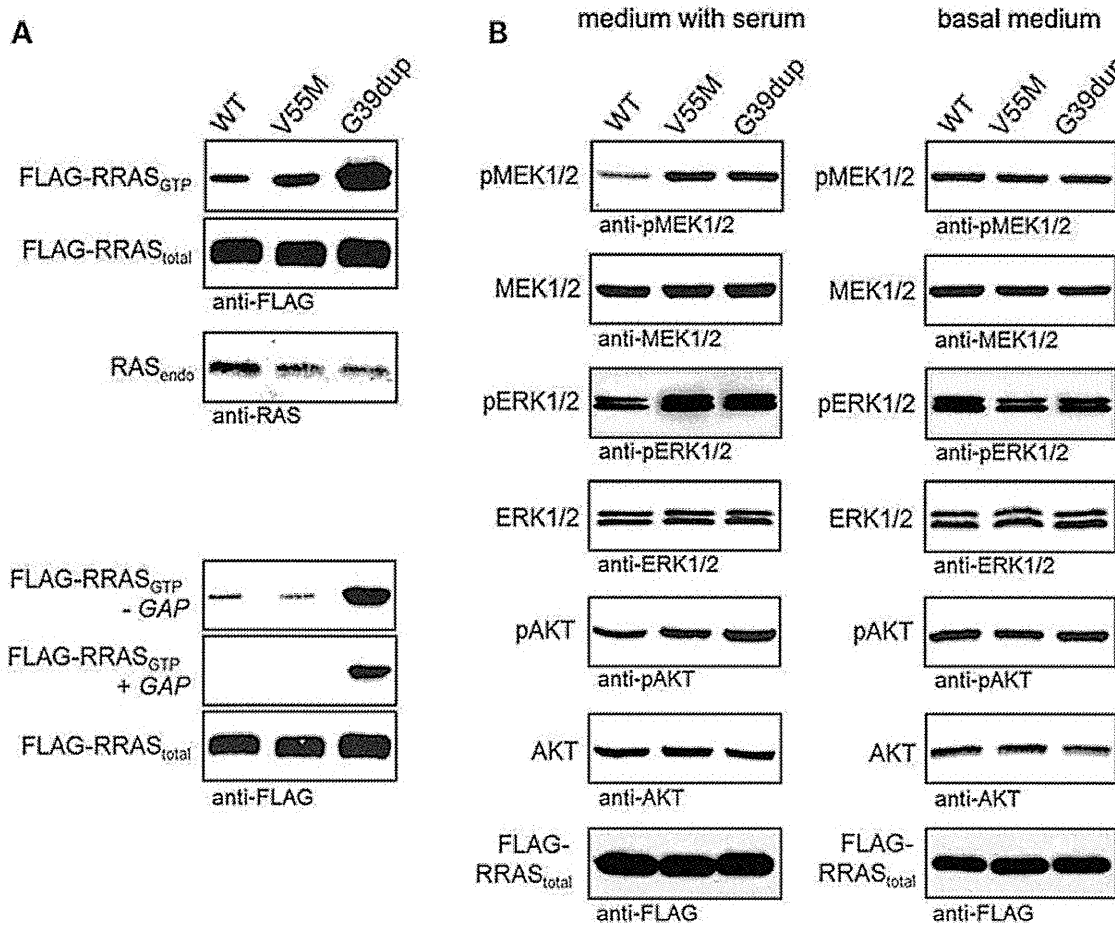

Figure 4. RRAS^{G39dup} and RRAS^{V55M} signalling activities in cells. (**A**) Determination of GTP-bound RRAS levels in COS-7 cells transiently expressing wild-type or mutant FLAG-tagged RRAS proteins. Assays were performed in the presence of serum (above), and in serum-free conditions (−GAP) or in the presence of the neurofibromin GAP domain (+GAP) (below). RRAS^{G39dup} was predominantly present in the active GTP-bound form and was resistant to GAP stimulation, whereas a slightly increased level of GTP-bound RRAS^{V55M} was observed in the presence of serum. Representative blots of three performed experiments are shown. (**B**) Determination of MEK, ERK and AKT phosphorylation levels (pMEK, pERK and pAKT) in transiently transfected COS-7 cells cultured in medium with serum (left) or basal medium (right). Expression of each RRAS mutant resulted in variably enhanced MEK, ERK and also partially AKT phosphorylation after stimulation. Total MEK, ERK and AKT in cell lysates are shown for equal protein expression and loading. Expression levels of exogenous, FLAG-tagged RRAS in cell lysates are shown for each experiment. Representative blots of three performed experiments are shown.

molecular cause underlying a group of clinically related developmental disorders, the RASopathies. Here, we used a gene candidacy approach based on large-scale protein–protein interaction/functional network analysis to identify *RRAS* as a novel gene implicated in a condition with features within the RASopathy spectrum. Disease-causing *RRAS* mutations are activating and act by maintaining the GTPase in its GTP-bound active state. Aberrant RRAS function was demonstrated to perturb variably intracellular signal flow through the RAF/MEK/ERK cascade, and to a certain extent also the PI3K/AKT pathway. Of note, these gain-of-function mutations are likely to define a novel leukaemia-prone condition. Consistent with this view, the same class of *RRAS* lesions was identified to occur as acquired somatic event in JMML, characterizing a subset of this myeloproliferative/myelodysplastic disorder with rapid progression to AML.

RRAS shares several biochemical properties with HRAS, NRAS and KRAS, as well as some common function, including stimulation of cell proliferation, survival and transformation (19,39). Despite these similarities, however, previous observations have emphasized the role of RRAS in cell adhesion, spreading and migration, and its modulatory function on effectors distinct from those used by 'classical' RAS proteins (40,41). While PI3K/AKT has been recognized as a major effector pathway of RRAS, only a minor impact on MAPK signalling had been reported (41,42). The present *in vitro* findings provide evidence that disease-associated RRAS mutants enhance the activation of the MAPK cascade, at least in response to specific stimuli. On the other hand, the identification of *RRAS* as a novel disease gene implicated in a RASopathy disorder further emphasizes the relevance of dysregulated signalling controlling cell spreading and migration in certain features of NS (e.g. congenital heart defects and lymphedema) and JMML (leukocyte infiltration in non-haematopoietic tissues) (43–45).

Caenorhabditis elegans studies provided evidence for a genetic interaction between the RAS-1^{G27dup}/RRAS^{G39dup} and

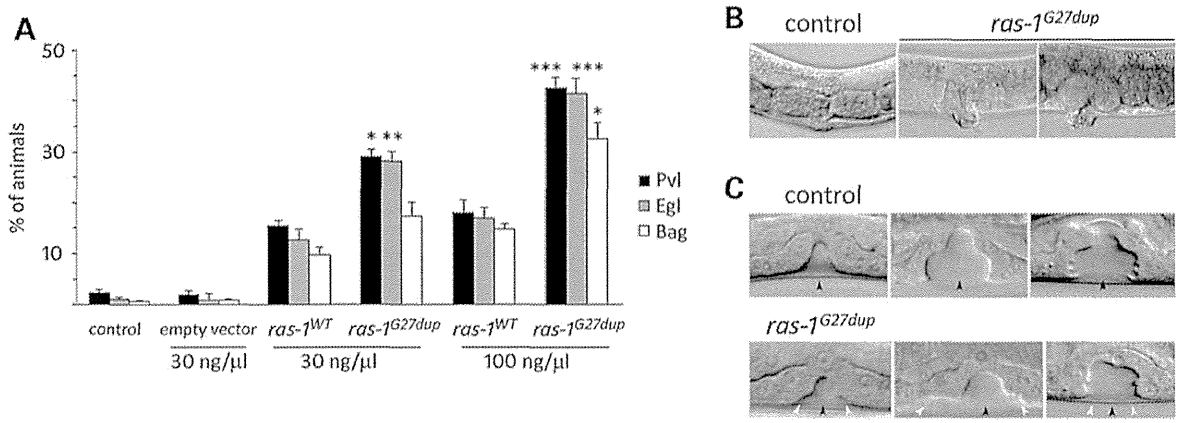

Figure 5. Consequences of *ras-1*^{G27dup} expression on *C. elegans* vulval development. (**A**) Heat-shock-driven expression of *ras-1*^{WT} and *ras-1*^{G27dup} at early L3 stage results in protruding vulva (Pvl), egg laying defective (Egl) and bag-of-worms (Bag) phenotypes. Isogenic animals that had lost the transgene (control group) and worms expressing the heat shock-inducible vector (empty vector) were subjected to heat shock and scored in parallel for comparison. The dose at which the transgene has been injected is reported at the bottom. Error bars indicate SD of three independent experiments. Asterisks indicate significant differences compared with *ras-1*^{WT} at the corresponding dose of injection ($^{*}P < 0.05$; $^{**}P < 0.005$; $^{***}P < 0.0005$; Fisher's Exact Test). (**B**) A proper vulva develops in heat-shocked control animals (left), whereas a protruding vulva is observed in heat-shocked *ras-1*^{G27dup} young adults (middle) and adult worms (right). (**C**) Nomarski images of vulval precursor cells in late L3 (left), early L4 (middle) and mid-late L4 (right) stages from synchronized animals heat-shocked at early L3. In control animals ($N = 48$), only P6.p descendants invaginate (upper panel), whereas in 10 of 30 analysed *ras-1*^{G27dup}-expressing worms, P5.p and/or P7.p descendants also detach from the cuticle, generating asymmetric invaginations (lower panel). Black arrowheads point to P6.p descendant invagination, whereas white arrowheads point to P5.p and P7.p descendant invagination. Anterior is to the left and dorsal is up, in all images.

LET-60/RAS *in vivo*. Specifically, expression of the RAS-1 mutant protein was able to rescue, in part, the VPC induction defect resulting from a hypomorphic LET-23 mutant and enhanced the multivulva phenotype associated with a LET-60 gain-of-function genetic background. No impact of wild-type RAS-1/RRAS expression was observed in both models. We also observed that worms expressing *ras-1*^{G27dup} displayed abnormal vulval morphogenesis (protruding vulva), possibly resulting from aberrant morphogenetic movements of the VPC descendant cells. Of note, we observed an equivalent phenotype in transgenic lines expressing SHOC2^{S2G} (38) and a PTPN11/SHP2 gain-of-function mutant (our unpublished data), suggesting functional equivalence of these mutants. Genetic studies support the view that these vulva defects arise, in part, through perturbation of signalling mediated by the RHO-related GTPase, RAC, which plays a critical role in vulval morphogenesis (37). This finding is in line with the established role of RRAS on RAC signalling (40,41) and with preliminary data indicating enhanced migration and chemotactic capabilities in cells stably expressing the disease-associated RRAS mutants (our unpublished data).

The biochemical characterization of disease-associated *RRAS* mutations provided strong evidence for the existence of distinct structural and mechanistic effects resulting in an overall enhancement of RRAS signalling. Function of RAS family proteins in signal transduction is controlled by two events, the GDP/GTP exchange and GTP hydrolysis. Any perturbation of these processes can affect dramatically the fine-tuned balance of the GTPase interaction with effectors and signal output. The majority of gain-of-function mutations affecting RAS proteins, including those contributing to oncogenesis, trigger the accumulation of these GTPases in the active state by impairing intrinsic GTPase activity, and/or conferring resistance to GAPs (17). This is also the case of two of the three mutations identified in this study, p.Gly39dup and p.Gln87Leu, the latter corresponding to the p.Gln61Leu in RAS proteins (present study and ref. 18,19). The characterization of the biochemical behaviour of RRAS^{G39dup}, however, also demonstrated a dramatic increase in both the intrinsic and GEF-catalysed nucleotide exchange as a process contributing to the accumulation of this mutant in its GTP-bound state. Aberrant GEF-accelerated nucleotide exchange dynamics was identified as the event driving functional dysregulation in the RRAS^{V55M} mutant, which was documented to be hyper responsive to GEF stimulation, but retained stimulus-dependency. Remarkably, the RRAS^{G39dup} and RRAS^{V55M} mutants were demonstrated to exhibit a diverse binding behaviour to effectors suggesting a differential impact of mutations on downstream signalling cascades, including PI3K/AKT and RALGDS/RAL, whose biological significance and impact, however, require further studies.

The clinical phenotype of the two subjects with germline *RRAS* mutations was reminiscent of NS. The individual with the Gly^{39} duplication displayed pulmonic stenosis, reduced growth, café-au-lait spots, mild motor delay and low-set ears, which recur in NS (5). Facial features, however, were distinctive, and not typical of NS. In contrast, the patient heterozygous for the p.Val55Met substitution exhibited a very mitigated phenotype characterized by suggestive facial characteristics (triangular face, downslanting palpebral fissures and low-set ears), low posterior hairline, broad chest and borderline cognitive abilities, without cardiac involvement or defective growth, indicating that clinical features associated with *RRAS* mutations might be quite subtle. Of note, the milder phenotype associated with the p.Val55Met change is consistent with the weaker perturbing effect of the RRAS^{V55M} mutant on MAPK and PI3K/AKT signalling compared with the RRAS^{G39dup} protein. Additional information on the spectrum of germline *RRAS* mutations, their associated phenotype and their functional impact on signalling,

Table 1. Vulva phenotypes in *C. elegans* mutant strains expressing wild-type RAS-1 or the disease-associated RAS-1^{G27dup} mutant

Genotype	Transgene	*N*	Muv (%)	Vul (%)	Pvl (%)	*N*	P6.p induction (%)
wild-type	none	207	0	0	1.0	48	100
let-60(n1046)	none	201	77.9	–	0.5	50	100
let-60(n1046)	*ras-1^{wt}*	244	76.4	–	2.8	43	100
let-60(n1046)	*ras-1^{G27dup}*	231	87.1[a]	–	3.0	50	100
let-23(sy1)	none	194	–	87.8	3.6	178	13.4
let-23(sy1)	*ras-1^{WT}*	169	–	84.3	4.1	156	14.0
let-23(sy1)	*ras-1^{G27dup}*	282	–	83.3	10.3[b]	128	24.2[c]

Strains: *let-60(n1046)* is a gain-of-function allele of *let-60* (ortholog of the human *HRAS*, *KRAS* and *NRAS* genes); *let-23(sy1)* is a hypomorphic allele of *let-23* (ortholog of the human *EGFR* gene). *ras-1^{WT}* and *ras-1^{G27dup}* indicate *hsp-16.41::ras-1^{WT}*- and *hsp-16.41::ras-1^{G27dup}*-containing constructs injected at 100 ng/μl, respectively. After each cross, isogenic worms that had lost the transgene were cloned separately and used as controls.
Animals were grown at 20°C and heat-shocked in parallel at early L3 stage. *N* indicates the number of animals scored. Multivulva (Muv), vulvaless (Vul) and protruding vulva (Pvl) phenotypes are expressed as percentage of worms with ectopic pseudovulvae, animals lacking a vulva and adults with a protruding vulva, respectively. Induction of vulval cell fate is expressed as percentage of P6.p that has been induced to invaginate.
In all comparisons, *P*-values were calculated using two-tailed Fisher's exact test.
[a]Significantly different from *let-60(n1046)* ($P < 0.02$).
[b]Significantly different from *let-23(sy1)* ($P < 0.01$) and *let-23(sy1);ras-1^{WT}* ($P < 0.02$).
[c]Significantly different from *let-23(sy1)* ($P = 0.02$) and *let-23(sy1);ras-1^{WT}* ($P < 0.05$).

however, is necessary to establish clinically relevant genotype–phenotype correlations.

JMML is a clonal myeloproliferative/myelodysplastic disorder of childhood characterized by overproduction of immature myeloid cells that variably retain the capacity to differentiate. Upregulation of RAS/MAPK signalling owing to germline and somatic mutations in *PTPN11*, *NRAS*, *KRAS*, *NF1* and *CBL* is a major event implicated in this malignancy (13,46,47). Our data document that upregulated RRAS function represents a novel event contributing to JMML pathogenesis and/or disease progression. Notably, somatic *RRAS* mutations co-occurred with acquired *NRAS* lesions in atypical JMML characterized by late onset and rapid progression to AML. While JMML is generally an aggressive malignancy, a subset of *NRAS/KRAS* mutation-positive patients has been reported to exhibit a mild course, with spontaneous remission despite the *RAS*-mutated clone persisting for years (48–50, our unpublished data). This suggests that in some instances, certain *NRAS* mutations are not sufficient to support full leukaemogenesis, requiring synergism with a second RAS signalling targeting event. In line with this view, *NRAS* mutations have been documented to co-exist with defects in other RASopathy genes (e.g. *PTPN11*) in some cases resulting in a particularly aggressive disease resembling AML with myelodysplasia-related changes (51,52), as that observed in the present cases. Other studies, however, are required to appreciate more precisely the role of enhanced RRAS function in leukaemogenesis as well as its clinical relevance in haematological malignancies.

In conclusion, our findings document that germline activating mutations in *RRAS* underlie a condition within the RASopathy family that may resemble NS phenotypically. In the examined cohorts, *RRAS* lesions were found to account for only a small portion of cases, which might be related to their severe consequences on embryonic/foetal development and/or to the biased selection of the subjects included in this study. Based on the present findings, however, *RRAS* mutations are expected to be more common among subjects with clinical features only partially overlapping NS, and particularly in patients with syndromic JMML/AML not associated with mutations in the *PTPN11*, *NF1*, *CBL*, *KRAS* and *NRAS* genes. While further efforts are required to characterize more precisely the clinical impact of germline and somatic mutations affecting *RRAS*, our findings suggest an unpredicted role of this GTPase in development and haematopoiesis. Consistent with the recent identification of *RIT1* as disease gene implicated in a significant proportion of NS (9), our findings further extend the concept of 'RASopathy gene' to a transducer whose dysregulated function perturbs signal flow through the MAPK cascade but does not belong to the core RAS/MAPK signalling cassette.

MATERIALS AND METHODS

Selection of RASopathy candidate genes

A web-based tool, Genes2FANs (http://actin.pharm.mssm.edu/genes2FANs), using a large-scale protein–protein interaction network coupled to a panel of functional association networks (FANs) was utilized to build a subnetwork connecting proteins to the known RASopathy genes (i.e. *PTPN11*, *SOS1*, *NF1*, *SPRED1*, *CBL*, *NRAS*, *KRAS*, *HRAS*, *RAF1*, *BRAF*, *SHOC2*, *MAP2K1* and *MAP2K2*), as seed proteins. Gene Ontology (biological process tree), mammalian phenotype browser, and Connectivity Map (drug-associated gene expression signatures), ChEA and TRANSFAC (transcription factor networks) databases were selected to construct the functional subnetworks utilized for prioritization of candidates (15). The programme allows to calculate z-scores for intermediate nodes (i.e. candidates), which are ranked based on their connections to the seed proteins.

Subjects and mutation analysis

Three cohorts of patients were considered in the study. A first group including 96 subjects with clinical features within the RASopathy spectrum and without mutation in previously identified RASopathy genes (i.e. *CBL*, *PTPN11*, *SOS1*, *KRAS*, *HRAS*, *NRAS*, *RAF1*, *BRAF*, *SHOC2*, *MAP2K1* and *MAP2K2*) was screened for a selected panel of candidates. A second cohort including 408 subjects with NS or a closely related phenotype previously tested negative for mutations in a heterogeneous subset

of RASopathy genes was scanned for *RRAS* mutations. All subjects included in this cohort had been screened for mutations in *PTPN11*, *SOS1* and *RAF1* genes. In both cohorts, the clinical diagnosis was made on the basis of standardized clinical criteria assessed by experienced clinical geneticists and paediatricians. Clinical features for the majority of subjects satisfied diagnostic criteria reported for NS, LEOPARD syndrome and cardiofaciocutaneous syndrome (53–57), but individuals who lacked sufficient features for a definitive diagnosis were also included. *RRAS* mutation analysis was also carried out on a cohort including 110 subjects with non-syndromic JMML that had prospectively been collected and genotyped (58). Mutation screening was performed on the entire *RRAS* coding sequence and flanking intronic stretches (NC_000019.10, 49635295.. 49640143, complement; NM_006270.3; NP_006261.1) on genomic DNA extracted from circulating leukocytes (cohorts I, II and III) or bone marrow aspirates (cohort III) by denaturing high-performance liquid chromatography (DHPLC) (3100 or 3500HT WAVE DNA fragment analysis system, Transgenomic, Omaha, NE, USA) and/or direct bidirectional sequencing (ABI Prism 3130, 3730 and 3500 Genetic Analyzers; Applied Biosystems, Foster City, CA, USA). Primer pairs, PCR and DHPLC conditions are available upon request. dbSNP137 (http://www.ncbi.nlm.nih.gov/projects/SNP/snp_summary.cgi), HapMap (rel.27) (http://hapmap.ncbi.nlm.nih.gov/) and 1000 Genomes (http://www.1000genomes.org/) databases were used to annotate the identified sequence variants. SIFT (http://sift.jcvi.org/), PolyPhen-2 (http://genetics.bwh.harvard.edu/pph2/) and MutationTaster (http://www.mutationtaster.org/) were used to predict the functional impact of the identified variants. Paternity was confirmed by STR genotyping, using the PowerPlex 16 System (Promega). DNA from leukocytes, hair bulb cells, bone marrow aspirates and skin fibroblasts was extracted using standard protocols. DNA specimens were collected under Institutional Review Board-approved protocols. Informed consent for DNA storage and genetic analyses was obtained from all subjects. Permission was obtained to publish picture of patient 9802, whereas subject NS1166 denied consent for picture publication.

Exome sequencing

Targeted enrichment and massively parallel sequencing were performed on genomic DNA extracted from circulating leukocytes and fibroblasts of patient 9802. Exome capture was carried out using the SureSelect Human All Exon V4+UTRs (Agilent), and sequencing with a HiSeq2000 instrument (Illumina). Image analysis and base calling were performed using the Real Time Analysis (RTA) pipeline v. 1.14 (Illumina). Paired-end reads alignment to the reference human genome (UCSC GRCh37/hg19) and variant calling were carried out using the CASAVA v. 1.8 pipeline (Illumina). Variant annotation, SNP filtering (dbSNP135, 1000 Genomes, HapMap and IntegraGen Exome databases) and patient-matched germline variant filtering were attained using an in-house pipeline by IntegraGen (Evry, France).

Molecular dynamics analyses

Starting coordinates for MD simulations were obtained from the RRAS crystallographic structure in complex with GDP and Mg^{2+} (PDB: 2FN4; RCSB Protein Data Bank, http://www.rcsb.org/pdb/home/home.do). The *N*-terminus and *C*-terminus of RRAS, absent in the crystal, were not considered in simulations. Deep View software was used to add atoms missing in the PDB file, belonging to residues 31, 96, 114, 121 and 192 as well as to substitute residue 55 (simulation of the p.Val55Met mutant) (59). All MD simulations were performed with GROMACS 4.5 package, by using the GROMOS96 43a1 force field parameters for the protein. Parameters for GDP were taken from the GROMACS website (http://www.gromacs.org). Simulations were performed as previously described (60,61), except for some details. Briefly, the proteins were initially placed in a dodecahedral box, solvated with ~6700 SPC water molecules, and six Na^+ ions were added to neutralize the protein charge. Following initial energy minimization and a 100-ps MD run, during which the protein atoms were position restrained, the temperature of solute and solvent was raised from 50 to 300 K in a stepwise manner. 200-ns-long simulations were performed for wild-type RRAS and the RASopathy causative mutant. The particle mesh Ewald method was used to evaluate electrostatic interactions (62), whereas a cut-off scheme was employed for Van der Waals interactions. Temperature and pressure were kept constant at 300 K and 1 bar by using the Berendsen weak-coupling method (63), using separate temperature baths for protein–GDP complex and solvent, with a relaxation time of 0.1 ps for temperature and 1 ps for pressure. A time step of 2 fs was employed. Root mean square deviations were calculated according to standard definitions. UCSF Chimera (http://www.cgl.ucsf.edu/chimera/) was used for molecular graphics and structures superposition, by using the MatchMaker option.

Biochemical and functional characterization of RRAS mutants

The generation of constructs, and preparation and purification of proteins were as previously described (64). The intrinsic activities of the RAS proteins, their modulation by GEFs and GAPs and their interaction with different effector proteins were determined as described earlier (65,66). Dissociation of mantGDP from RAS proteins (0.1 μM) was measured in the presence of 20 μM GDP in 30 mM Tris–HCl, pH 7.5, 10 mM KH_2PO_4/K_2HPO_4, 5 mM $MgCl_2$, 3 mM dithioerythritol (DTE), at 25 °C, using a Perkin Elmer fluorimeter at 366 nm (excitation wavelength) and 450 nm (emission wavelength). Observed rate constants (k_{obs}) of dissociation were obtained by single exponential fitting of the data. GEF-accelerated mantGDP dissociation from RAS proteins (0.1 μM) was measured as mentioned earlier, in the presence of the catalytic domain of SOS1, Cdc25 (5 μM), using stopped-flow instrument.

The intrinsic GTPase reaction was performed by mixing 70 μM nucleotide-free RAS proteins (HRAS, $RRAS^{WT}$, $RRAS^{V55M}$ and $RRAS^{G39dup}$) with 50 μM GTP in 30 mM Tris–HCl, pH 7.5, 10 mM KH_2PO_4/K_2HPO_4, 10 mM $MgCl_2$, 3 mM DTE, at 25°C, using HPLC assay as previously described (67). Samples were taken at different time points and analysed by HPLC for their GDP and GTP contents to determine the relative GTP content [(GTP)/(GDP + GTP)]. Intrinsic GTP hydrolysis k_{obs} of proteins were obtained by single exponential fitting of the data. For determination of GAP (neurofibromin, residues

1–333)-stimulated GTPase activity, GDP bound to HRAS and RRAS proteins was exchanged with excess mantGTP in the presence of alkaline phosphatase. Unbound nucleotides were removed by NAP5 column, and the RAS/mantGTP proteins were snap-frozen in liquid nitrogen (66). GAP-stimulated GTP hydrolysis of RAS proteins (0.2 μM) was measured in 30 mM Tris–HCl, pH 7.5, 10 mM $MgCl_2$, 3 mM DTE at 25°C using a Hightech TgK Scientific stopped-flow instrument. Reactions measured the decrease in fluorescence owing to hydrolysis of mantGTP. This decay was fit by a single exponential.

Effector binding assays were performed in 30 mM Tris–HCl, pH 7.5, 100 mM NaCl, 5 mM $MgCl_2$, 3 mM DTE at 25°C using a Fluoromax 4 fluorimeter in polarization mode. Increasing amounts of GST-tagged RAS-binding domains (RBD) of RAS effectors were titrated to 0.3 μM mantGppNHp-bound RAS proteins resulting in an increase of polarization (64). The dissociation constants (K_d) were calculated by fitting the concentration-dependent binding curve using a quadratic ligand binding equation.

For cell-based assays, COS-7 cells were transiently transfected with FLAG-tagged $RRAS^{WT}$, $RRAS^{V55M}$ or $RRAS^{G39dup}$ by the DEAE-dextran method. For serum conditions, cells were incubated for 48 h in 10% FCS. In serum-starved conditions, serum was changed to basal medium midway between the transfection and harvesting. Transfected COS-7 cells were harvested and lysed in fishing buffer [50 mM Tris–HCl, pH 7.5, 2 mM $MgCl_2$, 100 mM NaCl, 1% IGEPAL CA-630, 10% glycerol, EDTA-free protease inhibitor cocktail (Roche, 1 tablet/50 ml buffer), 20 mM disodium β-glycerol phosphate and 1 mM Na_3VO_4]. Cleared cell lysates were incubated with GSH-beads loaded with GST-RAF1-RBD. GTP-bound proteins and total recombinant proteins were analysed by immunoblotting with anti-FLAG antibody. Antibodies against MEK1/2, ERK1/2, AKT, phospho-MEK1/2 (Ser217/221), phospho-ERK1/2 (Thr202/Tyr204) and phospho-AKT (Thr308) were purchased from Cell Signaling Technology (68).

Caenorhabditis elegans studies

Culture and maintenance of animals were as previously described (69). The *let-60(n1046)* (*let-60/RAS* gain-of-function allele) and *let-23(sy1)* (*let-23/EGFR* hypomorphic allele) strains were provided by the *Caenorhabditis Genetics Center* (University of Minnesota). The three-nucleotide insertion, c.81_82insGGC (*ras-1*^{G27dup}), corresponding to c.116_118dup in *RRAS*, was introduced in the wild-type cDNA (*ras-1*^{WT}) (*C. elegans* ORF clone AAB03320, Thermo Scientific) by site-directed mutagenesis (QuikChange Site-Directed Mutagenesis Kit, Stratagene). *ras-1* cDNAs were subcloned into the pPD49.83 heat shock-inducible vector (a gift of A. Fire, Stanford University School of Medicine). Germline transformation was performed as described (70). pJM371 plasmid [*pelt-2*::NLS::*RFP*] (a gift from J.D. McGhee, University of Calgary), which drives red fluorescent protein (RFP) expression in intestinal cell nuclei, was used as co-injection marker (30 ng/μl). Two different doses of constructs were injected (30 and 100 ng/μl). Animals from at least three independent transgenic lines for each construct and each dose of injection (i.e. six lines expressing *ras-1*^{WT} and six lines expressing *ras-1*^{G27dup}) were heat-shocked in parallel and scored blindly at a Leica MZ10F dissecting microscope to check for the presence of protruding vulvae (Pvl phenotype) and multiple ectopic pseudovulvae (Muv phenotype), count the number of eggs retained in the uterus (Egl phenotype) and identify animals that had become bag-of-worms (Bag phenotype). Isogenic worms that had lost the transgene were cloned separately and used as controls. Following heat shock, all the transgenic lines expressing *ras-1*^{WT} or *ras-1*^{G27dup} showed a variable degree of these phenotypes. Lines *gbEx555a*[*hsp-16.41*::*ras-1*^{WT};*pelt-2*::NLS::*RFP*] and *gbEx557a*[*hsp-16.41*::*ras-1*^{G27dup};*pelt-2*::NLS::*RFP*] were scored quantitatively in triplicate experiments at the compound microscope and used for further analyses. Genetic crosses were performed according to standard methods (69). The genotype of individual alleles was confirmed by direct sequencing of the appropriate genomic region. After each cross, isogenic worms that had lost the transgene were used as controls.

To investigate VPCs induction and vulva morphogenesis, synchronized hermaphrodites carrying each transgene and the corresponding isogenic controls were heat-shocked in parallel at early L3 stage (33°C, 1 h, followed by 30°C, 1 h). Animals were scored at the compound microscope for vulval induction at late L3 and L4 stages, and for Pvl/Egl/Bag phenotypes at the adult stage. Microscopy observations were performed with a Nikon Eclipse 80i instrument equipped with Nomarski differential interference contrast optics on live animals mounted on 2% agarose pads containing 10 mM sodium azide as anaesthetic.

SUPPLEMENTARY MATERIAL

Supplementary Material is available at *HMG* online.

ACKNOWLEDGEMENTS

We are grateful to the participating patients and their families. We thank Serenella Venanzi (Istituto Superiore di Sanità, Rome, Italy), Michela Bonaguro (Policlinico S.Orsola-Malpighi, Bologna, Italy), Federica Consoli (Istituto Mendel, Rome, Italy) and Cédric Vignal and Sabrina Pereira (Hôpital Robert Debré, Paris, France) for skilful technical assistance, and the Open Laboratory (IGB-CNR, Naples, Italy) for experimental support. We also thank Paolo Bazzicalupo (IGB-CNR) for critical reading of the manuscript, paediatricians from the *Société Française des Cancers de l'Enfant* (SFCE) for providing biological material from their patients and CINECA for computational resources. Some nematode strains used in this work were provided by the *Caenorhabditis Genetics Center* (University of Minnesota, Minneapolis, MN, USA) funded by the NIH Office of Research Infrastructure Programs (P40OD010440).

Conflict of Interest statement. None declared.

FUNDING

This work was supported by grants from the ERA-Net for research programmes on rare diseases 2009 (NSEuroNet to M.Z., H.C., M.R.A. and M.T.), Telethon-Italy (GGP10020 and GGP13107 to M.T.), AIRC (IG 13360 to M.T.), NGFNplus program of the German Ministry of Science and Education (01GS08100 to M.R.A.), German Research Foundation through the Collaborative Research Center 974 (Communication and Systems Relevance

during Liver Injury and Regeneration to M.R.A.) and NIH (HL071207 to B.D.G.). F.P. was recipient of a research fellowship from '*Associazione Italiana Sindromi di Costello e cardiofaciocutanea*'. Funding to pay the Open Access publication charges for this article was provided by Telethon-Italy.

REFERENCES

1. Mitin, N., Rossman, K.L. and Der, C.J. (2005) Signaling interplay in Ras superfamily function. *Curr. Biol.*, **15**, R563–R574.
2. Mendoza, M.C., Er, E.E. and Blenis, J. (2011) The Ras-ERK and PI3K-mTOR pathways: cross-talk and compensation. *Trends Biochem. Sci.*, **36**, 320–328.
3. Harris, T.J.R. and McCormick, F. (2010) The molecular pathology of cancer. *Nat. Rev. Clin. Oncol.*, **7**, 251–265.
4. Pylayeva-Gupta, Y., Grabocka, E. and Bar-Sagi, D. (2011) RAS oncogenes: weaving a tumorigenic web. *Nat. Rev. Cancer*, **11**, 761–774.
5. Roberts, A.E., Allanson, J.E., Tartaglia, M. and Gelb, B.D. (2013) Noonan syndrome. *Lancet*, **381**, 333–342.
6. Schubbert, S., Shannon, K. and Bollag, G. (2007) Hyperactive Ras in developmental disorders and cancer. *Nat. Rev. Cancer*, **7**, 295–308.
7. Tartaglia, M. and Gelb, B.D. (2010) Disorders of dysregulated signal traffic through the RAS-MAPK pathway: phenotypic spectrum and molecular mechanisms. *Ann. N. Y. Acad. Sci.*, **1214**, 99–121.
8. Rauen, K.A. (2013) The RASopathies. *Annu. Rev. Genomics Hum. Genet.*, **14**, 355–369.
9. Aoki, Y., Niihori, T., Banjo, T., Okamoto, N., Mizuno, S., Kurosawa, K., Ogata, T., Takada, F., Yano, M., Ando, T. *et al.* (2013) Gain-of-function mutations in RIT1 cause Noonan syndrome, a RAS/MAPK pathway syndrome. *Am. J. Hum. Genet.*, **93**, 173–180.
10. Tartaglia, M., Gelb, B.D. and Zenker, M. (2011) Noonan syndrome and clinically related disorders. *Best Pract. Res. Clin. Endocrinol. Metab.*, **25**, 161–179.
11. Kratz, C.P., Rapisuwon, S., Reed, H., Hasle, H. and Rosenberg, P.S. (2011) Cancer in Noonan, Costello, cardiofaciocutaneous and LEOPARD syndromes. *Am. J. Med. Genet. C Semin. Med. Genet.*, **157C**, 83–89.
12. Gripp, K.W. (2005) Tumor predisposition in Costello syndrome. *Am. J. Med. Genet. C Semin. Med. Genet.*, **137C**, 72–77.
13. Loh, M.L. (2011) Recent advances in the pathogenesis and treatment of juvenile myelomonocytic leukaemia. *Br. J. Haematol.*, **152**, 677–687.
14. McKay, M.M. and Morrison, D.K. (2007) Integrating signals from RTKs to ERK/MAPK. *Oncogene*, **26**, 3113–3121.
15. Dannenfelser, R., Clark, N.R. and Ma'ayan, A. (2012) Genes2FANs: connecting genes through functional association networks. *BMC Bioinformatics*, **13**, 156.
16. Lowe, D.G., Capon, D.J., Delwart, E., Sakaguchi, A.Y., Naylor, S.L. and Goeddel, D.V. (1987) Structure of the human and murine R-ras genes, novel genes closely related to ras proto-oncogenes. *Cell*, **48**, 137–146.
17. Wennerberg, K., Rossman, K.L. and Der, C.J. (2005) The Ras superfamily at a glance. *J. Cell Sci.*, **118**, 843–846.
18. Krengel, U., Schlichting, I., Scherer, A., Schumann, R., Frech, M., John, J., Kabsch, W., Pai, E.F. and Wittinghofer, A. (1990) Three-dimensional structures of H-ras p21 mutants: molecular basis for their inability to function as signal switch molecules. *Cell*, **62**, 539–548.
19. Saez, R., Chan, A.M., Miki, T. and Aaronson, S.A. (1994) Oncogenic activation of human R-ras by point mutations analogous to those of prototype H-ras oncogenes. *Oncogene*, **9**, 2977–2982.
20. Aoki, Y., Niihori, T., Kawame, H., Kurosawa, K., Ohashi, H., Tanaka, Y., Filocamo, M., Kato, K., Suzuki, Y., Kure, S. *et al.* (2005) Germline mutations in HRAS proto-oncogene cause Costello syndrome. *Nat. Genet.*, **37**, 1038–1040.
21. Bollag, G., Adler, F., elMasry, N., McCabe, P.C., Conner, E. Jr, Thompson, P., McCormick, F. and Shannon, K. (1996) Biochemical characterization of a novel KRAS insertion mutation from a human leukemia. *J. Biol. Chem.*, **271**, 32491–32494.
22. Reimann, C., Arola, M., Bierings, M., Karow, A., van den Heuvel-Eibrink, M.M., Hasle, H., Niemeyer, C.M. and Kratz, C.P. (2006) A novel somatic K-Ras mutation in juvenile myelomonocytic leukemia. *Leukaemia*, **20**, 1637–1638.
23. Murugan, A.K., Hong, N.T., Cuc, T.T., Hung, N.C., Munirajan, A.K., Ikeda, M.A. and Tsuchida, N. (2009) Detection of two novel mutations and relatively high incidence of H-RAS mutations in Vietnamese oral cancer. *Oral. Oncol.*, **45**, e161–e166.
24. Sartori, G., Cavazza, A., Sgambato, A., Marchioni, A., Barbieri, F., Longo, L., Bavieri, M., Murer, B., Meschiari, E., Tamberi, S. *et al.* (2009) EGFR and K-ras mutations along the spectrum of pulmonary epithelial tumors of the lung and elaboration of a combined clinicopathologic and molecular scoring system to predict clinical responsiveness to EGFR inhibitors. *Am. J. Clin. Pathol.*, **131**, 478–489.
25. Milburn, M.V., Tong, L., deVos, A.M., Brünger, A., Yamaizumi, Z., Nishimura, S. and Kim, S.-H. (1990) Molecular switch for signal transduction: structural differences between active and inactive forms of protooncogenic ras proteins. *Science*, **247**, 939–945.
26. Diaz, J.F., Wroblowski, B., Schlitter, J. and Engelborghs, Y. (1997) Calculation of pathways for the conformational transition between the GTP- and GDP-bound states of the Ha-ras-p21 protein: calculations with explicit solvent simulations and comparison with calculations in vacuum. *Proteins*, **28**, 434–451.
27. Kuppens, S., Díaz, J.F. and Engelborghs, Y. (1999) Characterization of the hinges of the effector loop in the reaction pathway of the activation of ras-proteins. Kinetics of binding of beryllium trifluoride to V29G and I36G mutants of Ha-ras-p21. *Prot. Sci.*, **8**, 1860–1866.
28. Ma, J. and Karplus, M. (1997) Molecular switch in signal transduction: reaction paths of the conformational changes in ras p21. *Proc. Natl. Acad. Sci. USA*, **94**, 11905–11910.
29. Gorfe, A.A., Grant, B.J. and McCammon, J.A. (2008) Mapping the nucleotide and isoform-dependent structural and dynamical features of Ras proteins. *Structure*, **16**, 885–896.
30. Hall, B.E., Yang, S.S., Boriack-Sjodin, P.A., Kuriyan, J. and Bar-Sagi, D. (2001) Structure-based mutagenesis reveals distinct functions for Ras switch 1 and switch 2 in Sos-catalyzed guanine nucleotide exchange. *J. Biol. Chem.*, **276**, 27629–27637.
31. Suzuki, J., Kaziro, Y. and Koide, H. (1997) An activated mutant of R-Ras inhibits cell death caused by cytokine deprivation in BaF3 cells in the presence of IGF-I. *Oncogene*, **15**, 1689–1697.
32. Scheffzek, K., Ahmadian, M.R., Kabsch, W., Wiesmüller, L., Lautwein, A., Schmitz, F. and Wittinghofer, A. (1997) The Ras-RasGAP complex: structural basis for GTPase activation and its loss in oncogenic Ras mutants. *Science*, **277**, 333–338.
33. Lundquist, E.A. (2006) Small GTPases. In *WormBook*. The *C. elegans* Research Community, WormBook (ed.), http://www.wormbook.org. doi:/10.1895/wormbook.1.67.1.
34. Sternberg, P.W. (2005) Vulval development. In *Wormbook*. The *C. elegans* Research Community (ed.), http://www.wormbook.org. doi:10.1895/wormbook.1.6.1.
35. Sundaram, M.V. (2006) RTK/Ras/MAPK signaling. In *Wormbook*. The *C. elegans* Research Community (ed.), http://www.wormbook.org. doi/10.1895/wormbook.1.80.1.
36. Eisenmann, D.M. and Kim, S.K. (2000) Protruding vulva mutants identify novel loci and Wnt signaling factors that function during *Caenorhabditis elegans* vulva development. *Genetics*, **156**, 1097–1116.
37. Kishore, R.S. and Sundaram, M.V. (2002) ced-10 Rac and mig-2 function redundantly and act with unc-73 trio to control the orientation of vulval cell divisions and migrations in *Caenorhabditis elegans*. *Dev. Biol.*, **241**, 339–348.
38. Cordeddu, V., Di Schiavi, E., Pennacchio, L.A., Ma'ayan, A., Sarkozy, A., Fodale, V., Cecchetti, S., Cardinale, A., Martin, J., Schackwitz, W. *et al.* (2009) Mutation of SHOC2 promotes aberrant protein N-myristoylation and causes Noonan-like syndrome with loose anagen hair. *Nat. Genet.*, **41**, 1022–1026.
39. Cox, A.D., Brtva, T.R., Lowe, D.G. and Der, C.J. (1994) R-Ras induces malignant, but not morphologic, transformation of NIH3T3 cells. *Oncogene*, **9**, 3281–3288.
40. Wozniak, M.A., Kwong, L., Chodniewicz, D., Klemke, R.L. and Keely, P.J. (2005) R-Ras controls membrane protrusion and cell migration through the spatial regulation of Rac and Rho. *Mol. Biol. Cell*, **16**, 84–96.
41. Osada, M., Tolkacheva, T., Li, W., Chan, T.O., Tsichlis, P.N., Saez, R., Kimmelman, A.C. and Chan, A.M. (1999) Differential roles of Akt, Rac, and Ral in R-Ras-mediated cellular transformation, adhesion, and survival. *Mol. Cell. Biol.*, **19**, 6333–6344.
42. Marte, B.M., Rodriguez-Viciana, P., Wennström, S., Warne, P.H. and Downward, J. (1997) R-Ras can activate the phosphoinositide 3-kinase but not the MAP kinase arm of the Ras effector pathways. *Curr. Biol.*, **7**, 63–70.

43. Jopling, C., van Geemen, D. and den Hertog, J. (2007) Shp2 knockdown and Noonan/LEOPARD mutant Shp2-induced gastrulation defects. *PLoS Genet.*, **3**, e225.
44. Wang, S., Yu, W.M., Zhang, W., McCrae, K.R., Neel, B.G. and Qu, C.K. (2009) Noonan syndrome/leukemia-associated gain-of-function mutations in SHP-2 phosphatase (PTPN11) enhance cell migration and angiogenesis. *J. Biol. Chem.*, **284**, 913–920.
45. Chen, P.C., Wakimoto, H., Conner, D., Araki, T., Yuan, T., Roberts, A., Seidman, C., Bronson, R., Neel, B., Seidman, J.G. *et al.* (2010) Activation of multiple signalling pathways causes developmental defects in mice with a Noonan syndrome-associated Sos1 mutation. *J. Clin. Invest.*, **120**, 4353–4365.
46. Emanuel, P.D. (2008) Juvenile myelomonocytic leukemia and chronic myelomonocytic leukemia. *Leukemia*, **22**, 1335–1342.
47. Niemeyer, C.M. and Kratz, C.P. (2008) Paediatric myelodysplastic syndromes and juvenile myelomonocytic leukaemia: molecular classification and treatment options. *Br. J. Haematol.*, **140**, 610–624.
48. Matsuda, K., Shimada, A., Yoshida, N., Ogawa, A., Watanabe, A., Yajima, S., Iizuka, S., Koike, K., Yanai, F., Kawasaki, K. *et al.* (2007) Spontaneous improvement of hematologic abnormalities in patients having juvenile myelomonocytic leukemia with specific RAS mutations. *Blood*, **109**, 5477–5480.
49. Flotho, C., Kratz, C.P., Bergsträsser, E., Hasle, H., Starý, J., Trebo, M., van den Heuvel-Eibrink, M.M., Wójcik, D., Zecca, M., Locatelli, F. *et al.* (2008) Genotype-phenotype correlation in cases of juvenile myelomonocytic leukemia with clonal RAS mutations. *Blood*, **111**, 966–967.
50. Takagi, M., Piao, J., Lin, L., Kawaguchi, H., Imai, C., Ogawa, A., Watanabe, A., Akiyama, K., Kobayashi, C., Mori, M. *et al.* (2013) Autoimmunity and persistent RAS-mutated clones long after the spontaneous regression of JMML. *Leukaemia*, **27**, 1926–1928.
51. Park, H.D., Lee, S.H., Sung, K.W., Koo, H.H., Jung, N.G., Cho, B., Kim, H.K., Park, I.A., Lee, K.O., Ki, C.S. *et al.* (2012) Gene mutations in the Ras pathway and the prognostic implication in Korean patients with juvenile myelomonocytic leukemia. *Ann. Hematol.*, **91**, 511–517.
52. Sakaguchi, H., Okuno, Y., Muramatsu, H., Yoshida, K., Shiraishi, Y., Takahashi, M., Kon, A., Sanada, M., Chiba, K., Tanaka, H. *et al.* (2013) Exome sequencing identifies secondary mutations of SETBP1 and JAK3 in juvenile myelomonocytic leukemia. *Nat. Genet.*, **45**, 937–941.
53. Van der Burgt, I., Berends, E., Lommen, E., van Beersum, S., Hamel, B. and Mariman, E. (1994) Clinical and molecular studies in a large Dutch family with Noonan syndrome. *Am. J. Med. Genet.*, **53**, 187–191.
54. Allanson, J.E. (1987) Noonan syndrome. *J. Med. Genet.*, **24**, 9–13.
55. Sarkozy, A., Digilio, M.C. and Dallapiccola, B. (2008) LEOPARD syndrome. *Orphanet J. Rare Dis.*, **3**, 13.
56. Voron, D.A., Hatfield, H.H. and Kalkhoff, R.K. (1976) Multiple lentigines syndrome: case report and review of the literature. *Am. J. Med.*, **60**, 447–456.
57. Roberts, A., Allanson, J., Jadico, S.K., Kavamura, M.I., Noonan, J., Opitz, J.M., Young, T. and Neri, G. (2006) The cardiofaciocutaneous syndrome. *J. Med. Genet.*, **43**, 833–842.
58. Pérez, B., Kosmider, O., Cassinat, B., Renneville, A., Lachenaud, J., Kaltenbach, S., Bertrand, Y., Baruchel, A., Chomienne, C., Fontenay, M. *et al.* (2010) Genetic typing of CBL, ASXL1, RUNX1, TET2 and JAK2 in juvenile myelomonocytic leukaemia reveals a genetic profile distinct from chronic myelomonocytic leukaemia. *Br. J. Haematol.*, **151**, 460–468.
59. Guex, N. and Peitsch, M.C. (1997) SWISS-MODEL and the Swiss-PdbViewer: an environment for comparative protein modeling. *Electrophoresis*, **18**, 2714–2723.
60. Martinelli, S., Torreri, P., Tinti, M., Stella, L., Bocchinfuso, G., Flex, E., Grottesi, A., Ceccarini, M., Palleschi, A., Cesareni, G. *et al.* (2008) Diverse driving forces underlie the invariant occurrence of the T42A, E139D, I282V and T468M SHP2 amino acid substitutions causing Noonan and LEOPARD syndromes. *Hum. Mol. Genet.*, **17**, 2018–2029.
61. Bocchinfuso, G., Stella, L., Martinelli, S., Flex, E., Carta, C., Pantaleoni, F., Pispisa, B., Venanzi, M., Tartaglia, M. and Palleschi, A. (2007) Structural and functional effects of disease-causing amino acid substitutions affecting residues Ala72 and Glu76 of the protein tyrosine phosphatase SHP-2. *Proteins*, **66**, 963–974.
62. Darden, T., York, D. and Pedersen, L. (1993) Particle mesh Ewald: an N · log(N) method for Ewald sums in large systems. *J. Chem. Phys.*, **98**, 10089–10092.
63. Berendsen, H.J.C., Postma, J.P.M., van Gunsteren, W.F., Di Nola, A. and Haak, J.R. (1984) Molecular dynamics with coupling to an external bath. *J. Chem. Phys.*, **81**, 3684–3690.
64. Gremer, L., Merbitz-Zahradnik, T., Dvorsky, R., Cirstea, I.C., Kratz, C.P., Zenker, M., Wittinghofer, A. and Ahmadian, M.R. (2011) Germline KRAS mutations cause aberrant biochemical and physical properties leading to developmental disorders. *Hum. Mutat.*, **32**, 33–43.
65. Hemsath, L. and Ahmadian, M.R. (2005) Fluorescence approaches for monitoring interactions of Rho GTPases with nucleotides, regulators, and effectors. *Methods*, **37**, 173–182.
66. Jaiswal, M., Dubey, B.N., Koessmeier, K.T., Gremer, L. and Ahmadian, M.R. (2012) Biochemical assays to characterise Rho GTPases. *Methods Mol. Biol.*, **827**, 37–58.
67. Eberth, A. and Ahmadian, M.R. (2009) In vitro GEF and GAP assays. *Curr. Protoc. Cell Biol.*, **43**, 14.9.1–14.9.25.
68. Cirstea, I.C., Gremer, L., Dvorsky, R., Zhang, S.C., Piekorz, R.P., Zenker, M. and Ahmadian, M.R. (2013) Diverging gain-of-function mechanisms of two novel KRAS mutations associated with Noonan and cardio-facio-cutaneous syndromes. *Hum. Mol. Genet.*, **22**, 262–270.
69. Sulston, J.E. and Hodgkin, J. (1988) Methods. In Wood, W.B. and The Community of *C. elegans* Researchers (ed.), *The Nematode Caenorhabditis Elegans*. Cold Spring Harbor Laboratory Press, Cold Spring Harbor, NY, pp. 587–606.
70. Mello, C.C., Kramer, J.M., Stinchcomb, D. and Ambros, V. (1991) Efficient gene transfer in *C. elegans*: extrachromosomal maintenance and integration of transforming sequences. *EMBO J.*, **10**, 3959–3970.

Human Molecular Genetics, 2014, Vol. 23, No. 24 **6553–6566**
doi:10.1093/hmg/ddu376
Advance Access published on July 17, 2014

New *BRAF* knockin mice provide a pathogenetic mechanism of developmental defects and a therapeutic approach in cardio-facio-cutaneous syndrome

Shin-ichi Inoue[1], Mitsuji Moriya[1], Yusuke Watanabe[4], Sachiko Miyagawa-Tomita[5,6], Tetsuya Niihori[1], Daiju Oba[1], Masao Ono[2], Shigeo Kure[3], Toshihiko Ogura[4], Yoichi Matsubara[1,7] and Yoko Aoki[1,*]

[1]Department of Medical Genetics, [2]Department of Pathology, [3]Department of Pediatrics, Tohoku University School of Medicine, Sendai, Japan, [4]Department of Developmental Neurobiology, Institute of Development, Aging and Cancer, Tohoku University, Sendai, Japan, [5]Department of Pediatric Cardiology, [6]Division of Cardiovascular Development and Differentiation, Medical Research Institute, Tokyo Women's Medical University, Tokyo, Japan and [7]National Research Institute for Child Health and Development, Tokyo, Japan

Received March 15, 2014; Revised and Accepted July 14, 2014

Cardio-facio-cutaneous (CFC) syndrome is one of the 'RASopathies', a group of phenotypically overlapping syndromes caused by germline mutations that encode components of the RAS–MAPK pathway. Germline mutations in *BRAF* cause CFC syndrome, which is characterized by heart defects, distinctive facial features and ectodermal abnormalities. To define the pathogenesis and to develop a potential therapeutic approach in CFC syndrome, we here generated new knockin mice (here $Braf^{Q241R/+}$) expressing the *Braf* Q241R mutation, which corresponds to the most frequent mutation in CFC syndrome, Q257R. $Braf^{Q241R/+}$ mice manifested embryonic/neonatal lethality, showing liver necrosis, edema and craniofacial abnormalities. Histological analysis revealed multiple heart defects, including cardiomegaly, enlarged cardiac valves, ventricular noncompaction and ventricular septal defects. $Braf^{Q241R/+}$ embryos also showed massively distended jugular lymphatic sacs and subcutaneous lymphatic vessels, demonstrating lymphatic defects in RASopathy knockin mice for the first time. Prenatal treatment with a MEK inhibitor, PD0325901, rescued the embryonic lethality with amelioration of craniofacial abnormalities and edema in $Braf^{Q241R/+}$ embryos. Unexpectedly, one surviving pup was obtained after treatment with a histone 3 demethylase inhibitor, GSK-J4, or NCDM-32b. Combination treatment with PD0325901 and GSK-J4 further increased the rescue from embryonic lethality, ameliorating enlarged cardiac valves. These results suggest that our new *Braf* knockin mice recapitulate major features of RASopathies and that epigenetic modulation as well as the inhibition of the ERK pathway will be a potential therapeutic strategy for the treatment of CFC syndrome.

INTRODUCTION

Cardio-facio-cutaneous (CFC) syndrome is an autosomal dominant congenital anomaly syndrome, characterized by a distinctive facial appearance, short stature, congenital heart defects, intellectual disability and ectodermal abnormalities such as sparse, fragile hair, hyperkeratotic skin lesions and a severe generalized ichthyosis-like condition (1). The cardiac defects observed in CFC syndrome include pulmonary valve stenosis, hypertrophic cardiomyopathy and atrial septal defects. Increased nuchal translucency/fatal cystic hygroma colli due to lymphatic defects is also occasionally observed in affected individuals (2).

*To whom correspondence should be addressed at: Department of Medical Genetics, Tohoku University School of Medicine, 1-1 Seiryo-machi, Aoba-ku, Sendai 980-8574, Japan. Tel: +81 227178139; Fax: +81 227178142; Email: aokiy@med.tohoku.ac.jp

Our group as well as another group has identified germline *BRAF* mutations in 50–75% of patients with CFC syndrome (3–6). Other known CFC-causative genes include *KRAS* as well as *MAP2K1* and *MAP2K2* (MEK1 and MEK2, respectively) (3–6), all located in the same RAS–MAPK pathway that regulates cell differentiation, proliferation, survival and apoptosis (7). Germline mutations associated with RAS–MAPK pathway components cause partially overlapping disorders, including Noonan syndrome, Costello syndrome, LEOPARD syndrome, neurofibromatosis type 1 and Legius syndrome (neurofibromatosis type 1-like syndrome). These syndromes are now collectively termed RASopathies or RAS–MAPK syndromes (8–10).

BRAF is a serine threonine kinase which regulates the RAS–MAPK signaling pathway. Somatic *BRAF* mutations have been identified in 7% of human tumors, including melanoma, papillary thyroid carcinoma, colon cancer and ovarian cancer (11). The *BRAF* V600E mutation, located in the catalytic kinase domain (conserved region (CR) 3 domain), accounts for 90% of all somatic *BRAF* mutations. In contrast, *BRAF* V600E mutation has not been identified in CFC syndrome. Germline *BRAF* mutations in CR3 kinase domain, including G464R, G469E and L597V, were overlapping those in somatic mutations (4,5,12,13). In contrast, germline mutations in the CR1 domain have been rarely identified in somatic cancers. The most frequent mutations identified in CFC syndrome patients are substitutions of the residue Gln257 (p.Q257R and p.Q257K) in the CR1 domain, which account for ~40% (13). Previous studies have shown that the activation of downstream signaling, including ELK transactivation, is weaker in cells expressing the Q257R mutation than in those expressing V600E (3).

Braf is ubiquitously expressed in murine organs at mid-gestation, and high levels of its expression are found in the brain and testes at adult stage (14,15). *Braf* knockout mice have been found to die at mid-gestation from vascular defects due to enlarged blood vessels and apoptotic death of dif ferentiated endothelial cells (16). Heterozygous knockin mice constitutively expressing V600E mutation have been found to exhibit embryonic lethality (17). Knockin mice expressing a hypomorphic *BRAF* V600E allele have been reported to show phenotypes partially overlapping those of CFC syndrome patients, including small size, craniofacial abnormalities and epileptic seizures (18). However, no mouse model for CFC syndrome expressing a *Braf* mutation in the CR1 domain has been generated and no therapeutic approach has been developed. In the present study, we generated knockin mice expressing CFC syndrome-associated *Braf* Q241R mutation, corresponding to *BRAF* Q257R mutation, in order to investigate the molecular pathogenesis and potential therapeutic possibilities for CFC syndrome.

RESULTS

Generation of a CFC syndrome mouse model

We have previously reported that the transcriptional activity of ELK, downstream of ERK, was enhanced by the transient overexpression of human *BRAF* Q257R in NIH3T3 cells (3). To verify whether the expression of mouse *Braf* Q241R enhances ELK transcription as *BRAF* Q257R, reporter assays were performed in NIH3T3 cells. The expression of *Braf* Q241R and that of V637E, which corresponds to *BRAF* V600E, were ~2.7- and 8.4-fold higher than that of *Braf* WT, respectively (Fig. 1A). These results suggest that the *Braf* Q241R mutation is a gain-of-function mutation, although the activation is weaker than that observed in *Braf* V637E.

To investigate the gain-of-function effect of the *Braf* Q241R mutation on development, *Braf* Q241R knockin mice were generated (Fig. 1B). The targeting vector (Fig. 1B) was electroporated into ES cells and targeted clones were identified by Southern blotting (Fig. 1C). Appropriate ES cells were injected into BALB/c blastocysts and chimeras were obtained from six independent ES cell clones (hereafter referred to as $Braf^{Q241R\ Neo/+}$). To induce ubiquitous expression of *Braf* Q241R in germ cells, the $Braf^{Q241R\ Neo/+}$ mice were crossed with CAG-Cre transgenic mouse ($Braf^{+/+}$; *Cre*) and genotyping was confirmed by PCR (Supplementary Material, Fig. S1). Furthermore, sequencing was performed to confirm that Cre recombination resulted in *Braf* Q241R expression (Fig. 1D).

To examine if cell signaling pathways, including ERK, JNK, p38 and PI3K–AKT pathways, were altered in $Braf^{Q241R/+}$; *Cre* embryos, western blotting analysis was performed using cell extracts derived from whole-mouse embryos and brain. Protein levels of BRAF, CRAF, phosphorylated MEK and ERK in $Braf^{Q241R/+}$; *Cre* whole embryos were similar to those of $Braf^{+/+}$; *Cre* (Fig. 1E; Supplementary Material, Table S1), whereas phosphorylated MEK protein levels were higher in the brain of $Braf^{Q241R/+}$; *Cre* embryos (Fig. 1F; Supplementary Material, Table S2). Unexpectedly, phosphorylated p38 and AKT (Thr308) protein levels were somewhat lower in $Braf^{Q241R/+}$; *Cre* whole embryos at embryonic day (E) 14.5 (Fig. 1E; Supplementary Material, Table S1). These results suggest that $Braf^{Q241R/+}$; *Cre* embryos at E14.5 show a decrease of phosphorylated p38 and AKT (Thr308) protein levels.

Germline expression of *Braf* Q241R results in embryonic/neonatal lethality

Genotype analysis of embryos from an intercross between $Braf^{+/+}$; *Cre* and $Braf^{Q241R\ Neo/+}$ mice showed no surviving $Braf^{Q241R/+}$; *Cre* littermates at weaning, whereas $Braf^{+/+}$, $Braf^{+/+}$; *Cre* and $Braf^{Q241R\ Neo/+}$ littermates survived (Table 1). A normal Mendelian ratio was observed by E14.5. However, the survival rate of $Braf^{Q241R/+}$; *Cre* embryos dropped after E16.5. At E16.5, ~9.8% of embryos (4 of 41) were grossly hemorrhagic and edematous such as nuchal translucency (Fig. 2A, Table 1). Other $Braf^{Q241R/+}$; *Cre* embryos appeared normal (Fig. 2B) with no difference in body weight (data not shown). $Braf^{Q241R/+}$; *Cre* embryos, which were delivered by cesarean section at E18.5 and E19.5, remained pale and without movement or gasped for breath with cyanotic appearance, resulting in death within a few hours. A few embryos showed mandibular hypoplasia (2 of 39, 5.1%) and kyphosis (Fig. 2C and D).

Gross observation showed increased heart size in $Braf^{Q241R/+}$; *Cre* embryos at E16.5. At E18.5, $Braf^{Q241R/+}$; *Cre* embryos revealed severe peripheral liver necrosis (15 of 17, 88%) with decreased liver size and liver weight (Fig. 2E; Supplementary Material, Fig. S2). At E16.5, decreased liver weight was already observed (data not shown), although the gross appearance of the liver appeared normal. To examine if delayed lung maturation causes neonatal lethality, the histology of lung in

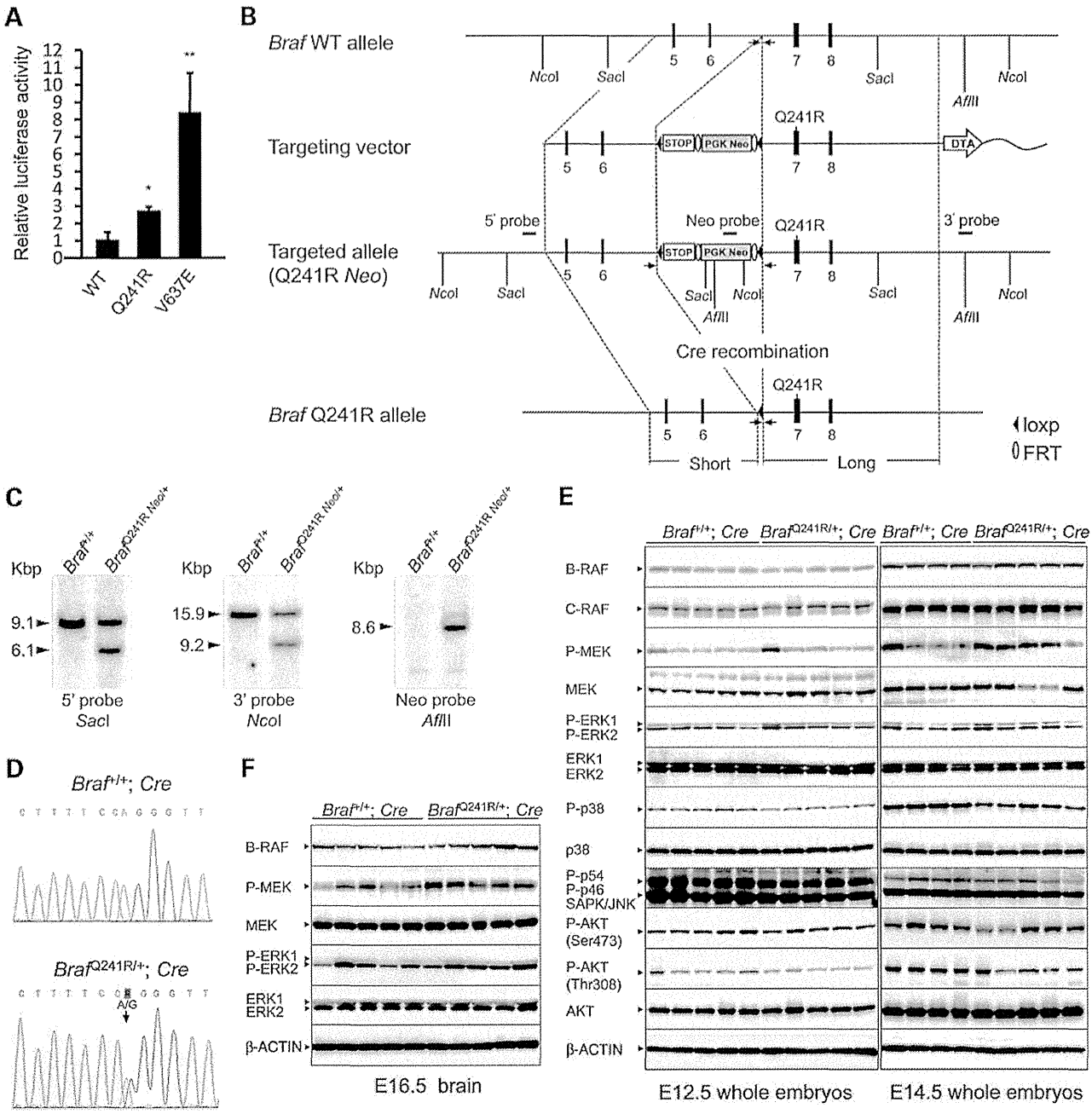

Figure 1. Generation of *Braf* Q241R knockin mice. (**A**) NIH 3T3 cells were transfected with the ELK1-GAL4 vector, the GAL4-luciferase trans-reporter vector, phRLnull-luc control vector and each mouse *Braf* expression plasmid, and reporter activities were determined as described in Materials and Methods. Luciferase activities were normalized with phRLnull-luc activities, containing distinguishable *R. reniformis* luciferase. Data are the means ± SD ($n = 4$). p.V637E in mouse *Braf* corresponds to oncogenic p.V600E in human *BRAF*. *, $P < 0.05$, **, $P < 0.01$ versus WT. WT, wild type. (**B**) Exons (solid boxes), PGK-Neomycin (PGK-Neo) cassette (gray box), STOP transcriptional sequences (open box), loxp sites (arrowheads) and Flp recombination target sites (ellipses) are indicated. Cleavage sites for diagnostic enzymes (*Sac*I, *Nco*I and *Afl*II) and the probes (5′-, 3′- and Neo probe) used to identify the homologous recombination are indicated. The PGK-Neo cassette was removed by crossing with CAG-Cre transgenic mice ($Braf^{+/+}$; *Cre*). The arrow indicates the positions of PCR primers used for genotyping of positive ES cells and mice. p. Q241R in mouse *Braf* corresponds to p.Q257R in human *BRAF*. DTA, diphtheria toxin A. (**C**) Southern blotting of ES cell clones. Genomic DNA from $Braf^{+/+}$ and $Braf^{Q241R\ Neo/+}$ ES cells was digested with *Sac*I (5′ probe), *Nco*I (3′ probe) or *Afl*II (Neo probe) and subjected to Southern blotting with a 5′, 3′ or Neo probe. The 5′, 3′ or Neo probe detects the 9.1-kb (*Braf* WT) and 6.1-kb ($Braf^{Q241R\ Neo/+}$) *Sac*I fragments, the 15.9 kb (*Braf* WT) and 9.2 kb ($Braf^{Q241R\ Neo/+}$) *Nco*I fragments or the 8.6 kb ($Braf^{Q241R\ Neo/+}$) *Afl*II fragment, respectively. (**D**) RNA was isolated from the brain of $Braf^{+/+}$; *Cre* and $Braf^{Q241R/+}$; *Cre* embryos at E18.5, and reverse transcribed into cDNA. Sanger sequencing was carried out using the cDNA. The arrow indicates the Q241R mutation in *Braf* exon 7. (**E** and **F**) Protein extracts from whole-mouse embryos (E12.5 and E14.5) and brain (E16.5) ($n = 4–5$ of each genotype) were subjected to western blotting with the indicated antibodies. β-Actin is shown as a loading control. The arrowheads indicate the bands corresponding to each protein.

Table 1. Genotyping of pups resulting from intercross between *Braf*$^{+/+}$; *Cre* and *Braf*$^{Q241R\ Neo/+}$ mice

Age	*Braf*$^{+/+}$	*Braf*$^{+/+}$; *Cre*	*Braf*$^{Q241R\ Neo/+}$	*Braf*$^{Q241R/+}$; *Cre*	*n*	*P*
E12.5	24	29	23	23	99	0.80
E13.5	5	14	6	6 (2 [1])	31	0.08
E14.5	19	22 (1)	23	11 (1 [1])	75	0.19
E16.5	57	60	55	34 (7 [4])	206	0.04
E18.5	16	23	20	0 (17 [4])	59	<0.0001
E19.5	11	16	11	0 (11 [1])	38	<0.01
Weaning (P21)	56	54	56	0	166	<0.0001
Expected	25%	25%	25%	25%		

Deviation from the expected Mendelian ratios was assessed by the χ^2 test. The number of dead embryos is shown in parentheses. The number of edematous embryos is shown in brackets. P: postnatal day.

Braf$^{Q241R/+}$; *Cre* embryos was examined at E18.5 and E19.5. Lungs of the mutant embryos appeared normal and were able to inflate, but ~11.1% of embryos (1 of 9) showed alveolar hemorrhage (Supplementary Material, Fig. S3). Thyroid transcription factor-1 (TTF-1; lung epithelial cells marker), pro-surfactant protein C and PAS staining showed similar levels in *Braf*$^{Q241R\ Neo/+}$ and *Braf*$^{Q241R/+}$; *Cre* embryos (Supplementary Material, Fig. S4), suggesting that lung development and maturation are normal. Gross observation suggests that *Braf*$^{Q241R/+}$; *Cre* embryos show embryonic/neonatal lethality, cardiomegaly, liver necrosis, edema and craniofacial abnormalities.

Braf$^{Q241R/+}$; *Cre* embryos display various heart defects

Because *Braf*$^{Q241R/+}$; *Cre* embryos showed cardiomegaly and liver necrosis, possibly due to heart failure (Fig. 2E), detailed histological analysis of the heart at different embryonic stages was conducted. At E12.5, the hearts of *Braf*$^{Q241R/+}$; *Cre* embryos appeared normal (Supplementary Material, Fig. S5A), but showed an enlarged pulmonary valve and a dramatic increase in the density of trabeculae (hypertrabeculation) at E14.5 (Supplementary Material, Fig. S5B). At E16.5, 13 of 14 (93%) *Braf*$^{Q241R/+}$; *Cre* embryos (excluding edematous embryos) had various heart defects (Supplementary Material, Tables S3 and S4). Hypertrophy of pulmonary, tricuspid and mitral valves was present in 7, 8 and 9 of 14 embryos, respectively (Fig. 3A; Supplementary Material, Tables S3 and S4). In particular, hypertrophy in pulmonary valve leaflets was prominent, plugging the entire space of the pulmonary valve ring (Fig. 3B). Other heart defects observed in *Braf*$^{Q241R/+}$; *Cre* embryos included ventricular septal defect (VSD) in 2 of 14 embryos (Fig. 3A), abnormal endocardial cushion in 2 (Fig. 3A), hypertrabeculation in 3 (Fig. 3A), epicardial blisters in 2 (Fig. 3A and C), a thickened trabecular layer and thinned compact layer in the left, right or combined myocardium (noncompaction: one case of cardiomyopathy accompanied by cardiac hypertrophy) in 4 (Fig. 3D) and hypoplasia of the coronary arteries in 3. The ventricular radius and the thickness of the pulmonary and tricuspid valves were significantly higher in *Braf*$^{Q241R/+}$; *Cre* embryos, suggesting cardiac enlargement and thickened pulmonary and tricuspid valves (Fig. 3E). These results suggest that *Braf*$^{Q241R/+}$; *Cre* embryos develop various congenital heart defects, which almost certainly contributes to embryonic lethality.

Braf$^{Q241R/+}$; *Cre* embryo hearts exhibit enhancement of cell proliferation, ERK signaling activation and decrease of phosphorylated p38 and AKT

To examine if heart defects observed in *Braf*$^{Q241R/+}$; *Cre* embryos are caused by increased cell proliferation and/or reduced cell death, cell proliferation was analyzed by phosphohistone H3 (pHH3) immunostaining and cell death by TUNEL assay. At E13.5, regarding heart abnormalities in each embryos, the number of pHH3-positive-stained cells varied. pHH3-positive-stained cells in the interventricular septum and myocardium increased in *Braf*$^{Q241R/+}$; *Cre* embryos (Fig. 4A and B). At E16.5, the nucleus of pHH3-positive cells increased in the interventricular septum in embryos with VSD (Fig. 4C). *Braf*$^{Q241R/+}$; *Cre* embryos had more pHH3-positive cells in pulmonary valves (Fig. 4D). In contrast to cell proliferation, hardly any cells undergoing apoptosis were observed in either *Braf*$^{+/+}$; *Cre* or *Braf*$^{Q241R/+}$; *Cre* at E13.5 and E16.5 (data not shown). These results suggest that the cell proliferation state depends on heart abnormalities in each embryo at E16.5 and that the increased staining for pHH3 in the interventricular septum was associated with VSD.

To examine if the cardiac signaling pathways were altered in *Braf*$^{Q241R/+}$; *Cre* embryos, the activation of kinases was screened in various signaling pathways using a phospho-kinase array followed by western blotting of the lysates from hearts of *Braf*$^{Q241R/+}$; *Cre* embryos at E16.5 (Fig. 4E and F; Supplementary Material, Fig. S6). No changes in phosphorylated ERK protein levels in both the phospho-kinase array and western blotting were observed. In contrast, phosphorylated p38, AKT (Ser473) and AKT (Thr308) protein levels, which are not direct targets of BRAF, were relatively lower in *Braf*$^{Q241R/+}$; *Cre* embryos than in *Braf*$^{+/+}$; *Cre*, which was confirmed by western blotting. To verify the activation of transcription factors downstream of ERK, the expression of ELK1 and the PEA3 (polyoma enhancer activator 3) subfamily Ets transcription factors were examined by quantitative real-time PCR, these expressions being known as transcriptional targets of FGF signaling-mediated activation of ERK in heart and oncogenic BRAF signaling in melanoma (19,20). At E13.5, E16.5 and E18.5, cardiac mRNA levels of *Etv1*, *Etv4* and *Etv5*, but not *Elk1*, were significantly higher in *Braf*$^{Q241R/+}$; *Cre* embryos than those in *Braf*$^{+/+}$; *Cre* (Fig. 4G; Supplementary Material, Fig. S7). Next, we investigated the influence of genes responsible for hypertrophic cardiomyopathy and

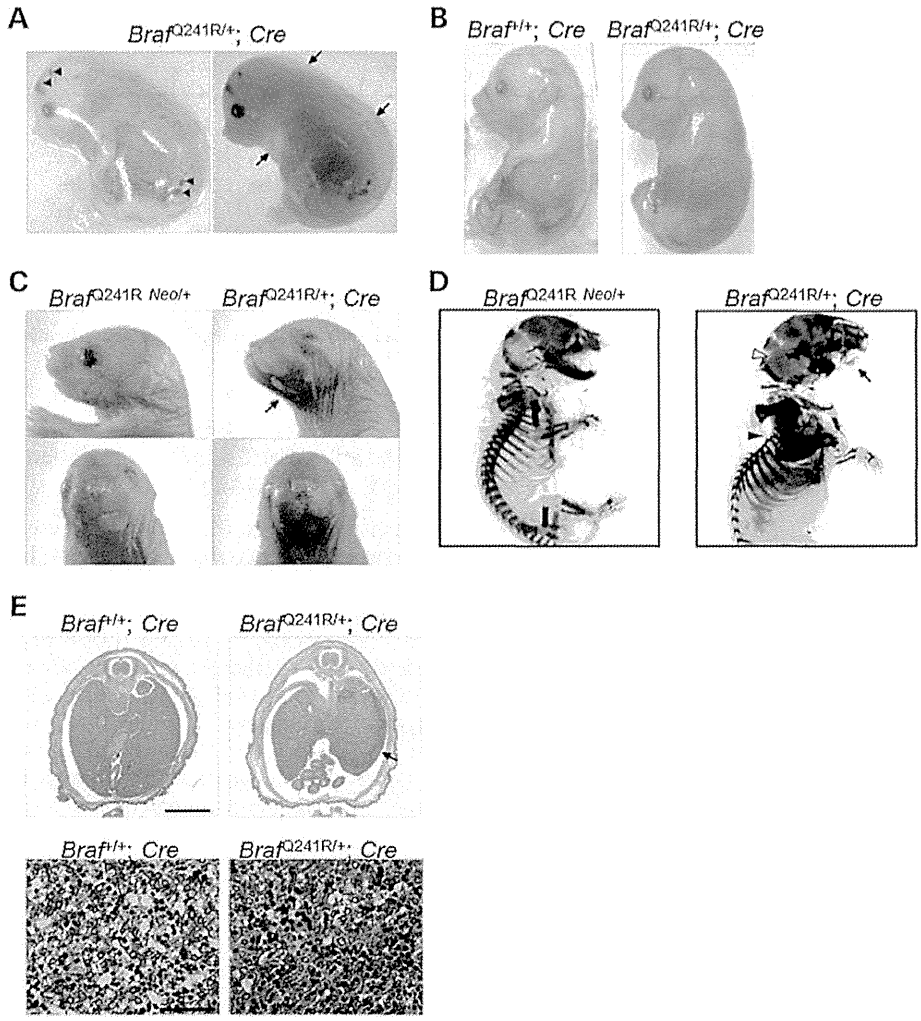

Figure 2. Lethal phenotypes of *Braf*$^{Q241R/+}$; *Cre* embryos. (**A** and **B**) Gross appearance of *Braf*$^{+/+}$; *Cre* and *Braf*$^{Q241R/+}$; *Cre* embryos at E16.5. (A) Arrowheads and arrows indicate hemorrhage and edema, respectively. The right panel shows *Braf*$^{Q241R/+}$; *Cre* embryos with transmitted illumination. (**C**) Craniofacial structure of *Braf*$^{Q241R\ Neo/+}$ and *Braf*$^{Q241R/+}$; *Cre* embryos at E19.5. The arrow indicates mandibular hypoplasia. (**D**) Alcian Blue/Alizarin Red staining of *Braf*$^{Q241R\ Neo/+}$ and *Braf*$^{Q241R/+}$; *Cre* embryos at E19.5. The arrow, solid arrowhead and open arrowhead indicate mandibular hypoplasia, kyphosis and ossification in the interparietal bone, respectively. (**E**) H&E staining of liver sections of *Braf*$^{+/+}$; *Cre* and *Braf*$^{Q241R/+}$; *Cre* embryos at E18.5. The arrow indicates hepatic necrosis. The lower panel shows higher magnification views of hepatic necrosis. Scale bars in upper panels = 200 μm and in lower panels = 50 μm.

cardiac development in *Braf*$^{Q241R/+}$; *Cre* embryos at E18.5, which exhibited a cardiomyopathy phenotype, such as cardiac enlargement and noncompaction (Fig. 3D and E) and structural abnormalities, including VSD. No differences in mRNA levels of cardiomyopathy-specific genes (*Myh6* and *Myh7)* and genes related to the heart formation and development (*Gata4* and *Nkx2.5*) were observed (Fig. 4G). These results suggest that ERK activation, including increased mRNA levels of Ets transcription factors, and decreased levels of p38 and AKT exist in heart tissues of *Braf*$^{Q241R/+}$; *Cre* embryos.

Braf$^{Q241R/+}$; *Cre* embryos develop lymphangiectasia

Patients with RASopathies, including CFC syndrome and Noonan syndrome, exhibit nuchal translucency, which is subcutaneous fluid collection in the fetal neck visualized by ultrasonography. Nuchal translucency is caused by distended jugular lymphatic sacs (JLSs), which result from a disturbance in differentiation of lymphatic endothelial cells (21,22). We hypothesized that the hemorrhage and edema in *Braf*$^{Q241R/+}$; *Cre* embryos may be caused by defective lymphatic development. Histological examination revealed distended and blood-filled JLSs in *Braf*$^{Q241R/+}$; *Cre* embryos but not in *Braf*$^{+/+}$; *Cre* embryos at E12.5 and E16.5 (Fig. 5A and B; Supplementary Material, Fig. S8A). The primary lymphatic sacs are remodeled to produce a hierarchically organized network of lymphatic capillaries and collecting lymph vessels at stages between E14.5 and postnatal stages (23). The JLSs are hardly observed in mouse embryos at E16.5. In *Braf*$^{Q241R/+}$; *Cre* embryos at E16.5, cavities such as the JLSs of mouse embryos from E12.5 to E14.5 were observed (Fig. 5B), suggesting defective lymphatic development from the cardinal vein in *Braf*$^{Q241R/+}$; *Cre*

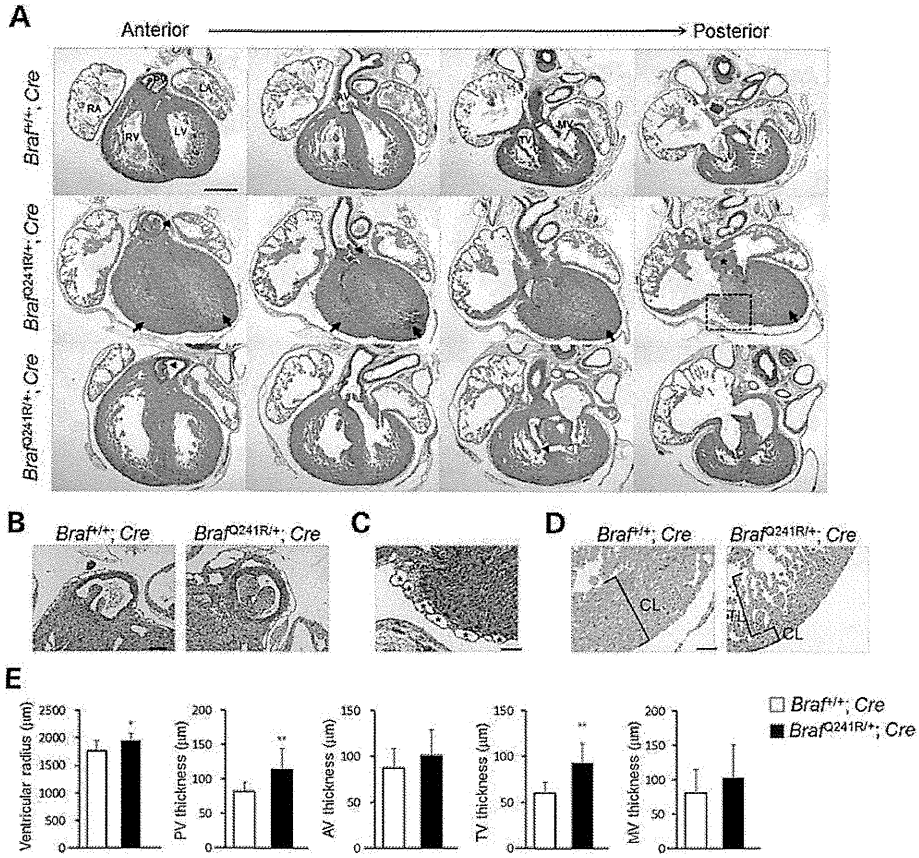

Figure 3. Cardiac phenotype of *Braf*$^{Q241R/+}$; *Cre* embryos. (**A**–**D**) H&E staining of sequential anterior to posterior sections of embryonic hearts from *Braf*$^{+/+}$; *Cre* and *Braf*$^{Q241R/+}$; *Cre* at E16.5. A dramatic increase in density of trabeculae (arrows), enlarged valves (solid arrowheads), VSD (open arrowhead) and abnormal endocardial cushion (asterisk) are observed. Scale bars 500 μm (A) and 100 μm (B–D). (B) Higher magnification of the pulmonary valves in *Braf*$^{+/+}$; *Cre* and *Braf*$^{Q241R/+}$; *Cre* embryos. (C) Higher magnification of the boxed region in Figure 3A showing the epicardial blisters (asterisks) in *Braf*$^{Q241R/+}$; *Cre* embryos at E16.5. (D) Representative image of noncompaction in hearts from *Braf*$^{Q241R/+}$; *Cre* embryos at E16.5. (**E**) The ventricular radius and the thicknesses of the cardiac valve leaflets were measured at their largest diameter in serial sections of *Braf*$^{+/+}$; *Cre* and *Braf*$^{Q241R/+}$; *Cre* embryos at E16.5. Data are the means ± SD (*Braf*$^{+/+}$; *Cre* ($n = 9$) and *Braf*$^{Q241R/+}$; *Cre* ($n = 14$)). $^{*}P < 0.05$, $^{**}P < 0.01$ versus *Braf*$^{+/+}$; *Cre*. LV, left ventricle; RV, right ventricle; LA, left atrium; RA, right atrium; PV, pulmonary valve; AV, aortic valve; TV, tricuspid valve; MV, mitral valve; CL, compact layer; TL, trabecular layer.

embryos. To examine the network formation of blood and lymphatic vessels, we performed immunostaining using antibodies against lymphatic vessel endothelial hyaluronan receptor 1 (LYVE-1; lymphatic endothelial cell-specific marker), α-SMA for staining of vessels with smooth muscle and CD31 (platelet-endothelial cell adhesion molecule-1, PECAM-1) for staining of vascular endothelial cells. At E12.5, the cells lining JLSs in both *Braf*$^{+/+}$; *Cre* and *Braf*$^{Q241R/+}$; *Cre* embryos were positive for LYVE-1 (Fig. 5C), whereas slightly CD31-positive cells were detected in JLSs and the jugular vein (Fig. 5D). No α-SMA expression was observed (Supplementary Material, Fig. S8B). At E16.5, the cavities such as the JLSs in *Braf*$^{Q241R/+}$; *Cre* embryos were negative for LYVE-1, α-SMA and CD31 (Fig. 5E; Supplementary Material, Fig. S8C and D), but the subcutaneous lymphatic vessels were markedly positive for LYVE-1 (Fig. 5F; Supplementary Material, Fig. S8E). These results indicate that *Braf*$^{Q241R/+}$; *Cre* embryos show defective lymphatic development from the cardinal vein, leading to distention of the JLSs, dilated lymphatic vessels and edema.

Treatment with a MEK inhibitor and/or histone demethylase inhibitors prevents embryonic lethality in *Braf*$^{Q241R/+}$; *Cre* embryos

MEK inhibitor, PD0325901, treatment is known to rescue the embryonic lethality of Noonan syndrome model mice (24). Pregnant *Braf*$^{+/+}$; *Cre* mice were treated with various compounds to see whether this would result in recovery from embryonic lethality (Table 2). Male *Braf*$^{Q241R\ Neo/+}$ mice were crossed with female *Braf*$^{+/+}$; *Cre* mice, and pregnant mice were intraperitoneally injected with dimethylsulfoxide (vehicle), PD0325901 [0.5 or 1.0 mg of body weight (mg/kg)], MAZ51 (VEGFR3 inhibitor; 1.0, 2.0 or 5.0 mg/kg), sorafenib (BRAF, VEGFR, PDGFR multikinase inhibitor; 5.0 mg/kg), lovasatin (HMG-CoA reductase and farnesyl transferase inhibitor; 5.0 mg/kg) or everolimus (mTOR inhibitor; 0.1 mg/kg), daily from E10.5 to E18.5. PD0325901 treatment (0.5 mg/kg) modestly rescued the embryonic lethality of *Braf*$^{Q241R/+}$; *Cre* mice (2 of 30). Seven embryos also survived for 3 weeks with

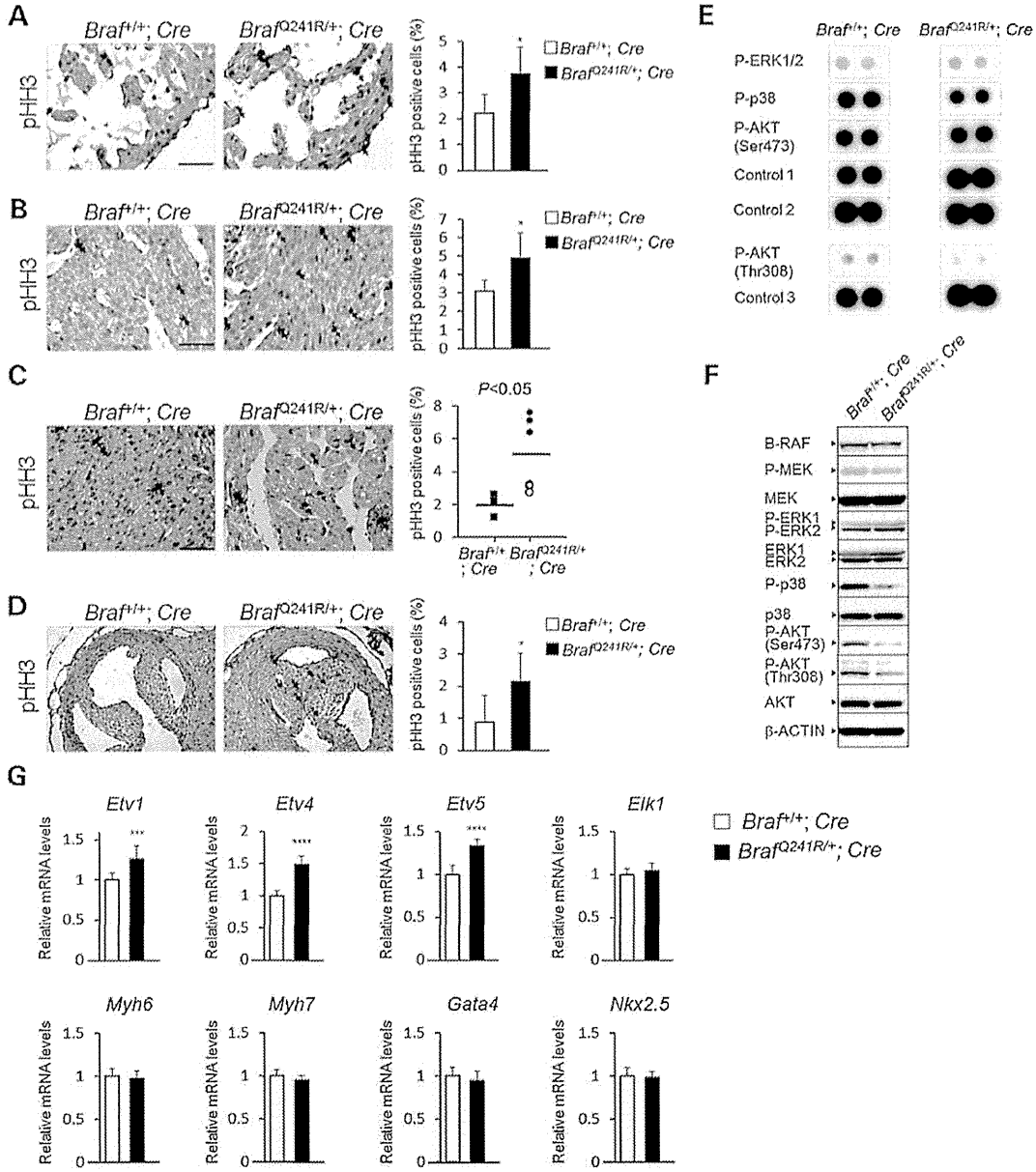

Figure 4. Increased cell proliferation and altered multiple signaling pathways in *Braf*$^{Q241R/+}$; *Cre* embryo hearts. (**A**–**D**) Immunostaining for pHH3 in the myocardium (A), interventricular septum (B and C) and pulmonary valves (D) of *Braf*$^{+/+}$; *Cre* and *Braf*$^{Q241R/+}$; *Cre* embryos at E13.5 (A and B) and E16.5 (C and D). The arrows indicate representative positive cells. *Braf*$^{Q241R/+}$; *Cre* embryos with or without VSD are shown in closed cycles or open circles, respectively. Scale bars 50 μm (A–C). Data are means ± SD (A and B) *Braf*$^{+/+}$; *Cre* ($n = 5$) and *Braf*$^{Q241R/+}$; *Cre* ($n = 5$). (C and D) *Braf*$^{+/+}$; *Cre* ($n = 3$) and *Braf*$^{Q241R/+}$; *Cre* ($n = 6$). $^{*}P < 0.05$ versus *Braf*$^{+/+}$; *Cre*. (**E**) Protein extracts (400 μg) of the hearts from *Braf*$^{+/+}$; *Cre* and *Braf*$^{Q241R/+}$; *Cre* embryos at E16.5 were subjected to Phospho-Kinase Antibody Array. Results are representative of gene spots that showed significant changes in 45 phosphorylated proteins. (**F**) Western blotting of the hearts from *Braf*$^{+/+}$; *Cre* and *Braf*$^{Q241R/+}$; *Cre* embryos at E16.5 (pooled samples; *Braf*$^{+/+}$; *Cre* ($n = 5$), *Braf*$^{Q241R/+}$; *Cre* ($n = 5$)). β-Actin is shown as a loading control. The arrowheads indicate the bands corresponding to each protein. (**G**) Cardiac mRNA levels were determined by quantitative reverse transcription–PCR. mRNA levels were normalized by those of *Gapdh*, and those in *Braf*$^{+/+}$; *Cre* at E18.5 are set at 1. Data are the means ± SD (*Braf*$^{+/+}$; *Cre* ($n = 10$) and *Braf*$^{Q241R/+}$; *Cre* ($n = 6$)). $^{***}P < 0.001$, $^{****}P < 0.0001$ versus *Braf*$^{+/+}$; *Cre*. *Etv1*, *Etv4*, *Etv5*, *Myh6* and *Myh7* encode ER81, Pea3, ERM, α-MHC and β-MHC, respectively.

prenatal treatment of PD0325901 (1.0 mg/kg) (7 of 37, $P = 0.32$, χ^2 test for deviation from the Mendelian ratios). PD0325901-treated *Braf*$^{Q241R/+}$; *Cre* embryos appeared normal without edema and mandibular hypoplasia (0 of 31 at E16.5 to P0), whereas other genotype mice, excluding *Braf*$^{Q241R/+}$; *Cre* treated with PD0325901, showed teratogenic effects, including open eyes (Supplementary Material, Fig. S9), edema, enlarged semilunar valves and atrioventricular valves (data not shown). Other compounds had no effect on the recovery of embryonic lethality in *Braf*$^{Q241R/+}$; *Cre* embryos.

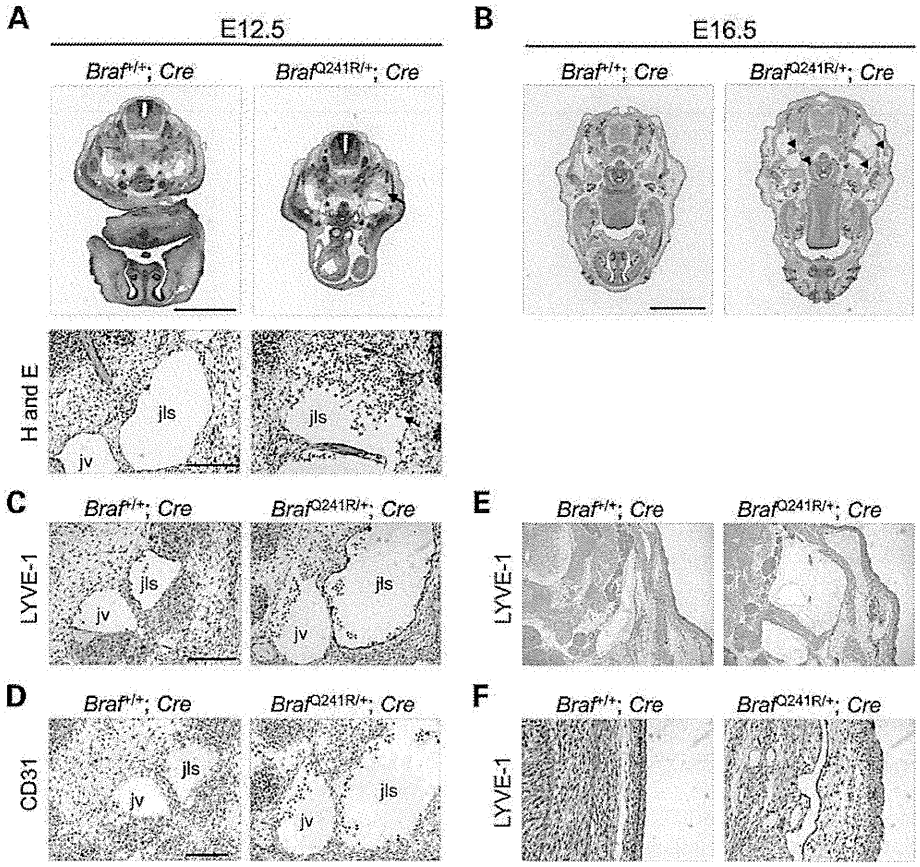

Figure 5. Abnormal lymphatic development in *Braf*$^{Q241R/+}$; *Cre* embryos. (**A** and **B**) Transverse sections of *Braf*$^{+/+}$; *Cre* and *Braf*$^{Q241R/+}$; *Cre* embryos at E12.5 (A) and E16.5 (B) stained with H&E. Lower panels show high-magnification views of jugular lymph sac (A). The arrows (A) and arrowheads (B) indicate blood cells in jugular lymph sacs and the regions which are similar to the jugular lymph sacs or jugular veins of embryos at E12.5, respectively. Scale bars 1 mm (in upper panels, A), 100 μm (in lower panels, A) and 2 mm (B). (**C**–**F**) Sections of *Braf*$^{+/+}$; *Cre* and *Braf*$^{Q241R/+}$; *Cre* embryos at E12.5 (C and D) and E16.5 (E and F) stained with antibodies against lymphatic endothelial markers, LYVE-1 (C, E and F) or CD31 (D). (F) Subcutaneous lymphatic vessels. jls, jugular lymph sac; jv, jugular vein.

Thus, PD0325901 treatment prevented embryonic lethality in *Braf*$^{Q241R/+}$; *Cre* embryos and could ameliorate edema and mandibular hypoplasia.

Epigenetic regulation of gene expression, such as histone acetylation and histone methylation, plays a crucial role in the transcriptional regulation of cell differentiation, development, the inflammatory response and cancer (25). Recently, a histone deacetylase inhibitor, SAHA [vorinostat (Zolinza)], has been used in the treatment of lymphomas and solid tumors. Recent studies have suggested the association of UTX and JMJD3, a histone H3 lysine 27 (H3K27) demethylase, with heart development (26–28). We therefore tested whether treatment using these compounds leads to the rescue of embryonic lethality (Table 2). SAHA treatment had no effect (data not shown); however, one embryo survived for 3 weeks with prenatal treatment of GSK-J4 (inhibitors of histone H3K27 demethylase UTX and JMJD3; 5.0 mg/kg) (25) or NCDM-32b (inhibitor of histone H3K9 demethylase JMJD2C; 5.0 mg/kg) (29). Moreover, co-treatment with GSK-J4 (5.0 mg/kg) and PD0325901 (0.5 mg/kg) further increased the number of *Braf*$^{Q241R/+}$; *Cre* mice alive at weaning (5 of 31, $P = 0.14$). The teratogenic effects, which were frequently observed in PD0325901 treatment, were not observed in the co-treatment with GSK-J4 and PD0325901.

We further investigated whether co-treatment with PD0325901 and GSK-J4 prevented heart defects in *Braf*$^{Q241R/+}$; *Cre* embryos. Co-treatment with PD0325901 and GSK-J4, but not PD0325901 treatment (1.0 mg/kg) alone, ameliorated enlarged pulmonary, tricuspid and mitral valves in *Braf*$^{Q241R/+}$; *Cre* embryos (Fig. 6A and B). However, no difference in the frequency of heart defects, including VSD, hypertrabeculation, epicardial blisters and noncompaction, was observed. It is noteworthy that treatment with PD0325901 or GSK-J4 alone or the co-treatment reversed the decrease of phosphorylated p38 protein levels (Fig. 6C; Supplementary Material, Fig. S10). These results suggest that combination treatment with PD0325901 and GSK-J4 prevents embryonic lethality, enlarged cardiac valves and decreased phosphorylated p38 in *Braf*$^{Q241R/+}$; *Cre* embryos.

DISCUSSION

In this study, we generated heterozygous *Braf* Q241R-expressing mice, which exhibited embryonic and postnatal lethality due to liver necrosis, skeletal abnormalities, lymphatic defects and various cardiac defects, including cardiomegaly, noncompaction, enlarged cardiac valves and hypertrabeculation.

Table 2. Rescue of embryonic lethality in *Braf*$^{Q241R/+}$; *Cre* embryos by MEK inhibitor, histone demethylase inhibitor or these combined treatment

Compound	Dose (mg/kg body weight)	Genotype (3 weeks) *Braf*$^{+/+}$	*Braf*$^{+/+}$; *Cre*	*Braf*$^{Q241R\ Neo/+}$	*Braf*$^{Q241R/+}$; *Cre*	n^a	n^b	n^c	*P*
DMSO (vehicle)	–	14	8	8	0	30	6	5.0	<0.01
PD0325901	0.5	7	14	7	2	30	13	2.3	0.02
	1.0	11	13	6	7	37	14	2.6	0.32
MAZ51	1.0	9	8	11	0	28	6	4.7	0.02
	2.0	10	14	7	0	31	6	5.2	<0.01
	5.0	10	7	11	0	28	11	2.5	0.01
Sorafenib	5.0	12	15	8	0	35	13	2.7	<0.01
Lovastatin	5.0	8	19	17	0	44	10	4.4	<0.01
Everolimus	0.1	6	6	9	0	21	9	2.3	0.04
NCDM-32b	2.0	12	4	9	0	25	9	2.8	<0.01
	5.0	10	10	14	1	35	11	3.2	0.02
	10.0	11	10	19	0	40	9	4.4	<0.01
GSK-J4	5.0	8	18	14	1	41	11	3.7	<0.01
	10.0	16	26	20	0	62	23	2.7	<0.01
PD0325901 + GSK-J4	0.5 + 5.0	8	13	5	5	31	10	3.1	0.14

Male *Braf*$^{Q241R\ Neo/+}$ mice were crossed with female *Braf*$^{+/+}$; *Cre* mice, and pregnant mice were intraperitoneally injected with vehicle or various compounds shown daily from E10.5 to E18.5. Deviation from the expected Mendelian ratios was assessed by χ^2 test. n^a, the total number of acquired pups. n^b, the total number of treated female *Braf*$^{+/+}$; *Cre* mice. n^c, the average number of survived pups at weaning (n^a/n^b).

Increased expression of Ets transcription factors and decreased expression of cardiac phosphorylated p38 in embryonic heart tissues were observed. PD0325901 treatment, in part, rescued embryonic and postnatal lethality in *Braf*$^{Q241R/+}$; *Cre* mice. One pup in *Braf*$^{Q241R/+}$; *Cre* also survived until P21 with treatment of GSK-J4 or NCDM-32b. PD0325901 treatment, but not GSK-J4 and NCDM-32b treatment, ameliorated edema and mandibular hypoplasia. Moreover, PD0325901 co-treatment with GSK-J4 further rescued embryonic lethality with recovered hypertrophy of pulmonary, tricuspid and mitral valves and the decreased expression of phosphorylated p38. Taken together, mice expressing a development-specific *Braf* Q241R mutation will be useful to further clarify the pathogenesis of CFC syndrome and to develop therapeutic approaches.

Patients with RASopathies are characterized by generalized abnormalities of lymphatic development. Fetuses with RASopathies have been shown to be characterized by hydrops, pleural effusions, increased nuchal translucency due to distended JLS and cystic hygroma in utero (30–32). Children and adults with RASopathies show generalized lymphedema, peripheral lymphoedema or pulmonary lymphangiectasia (33). Our new model, *Braf*$^{Q241R/+}$; *Cre* mice, showed embryonic and postnatal lethality and exhibited multiple developmental defects in the lymphatic system, including hydrops, distended JLS and subcutaneous lymphatic vessels. In contrast, mice of other knockin mouse models for RASopathies survived to adulthood and have not shown the defects in lymphatic system (34–36). Thus, for the first time our new model *Braf*$^{Q241R/+}$; *Cre* mice demonstrated the developmental lymphatic defects, which are the common features observed in RASopathies, in knockin mouse models for RASopathies.

Dysregulation of the RAS–MAPK pathway is a common underlying mechanism of RASopathies. However, a variety of compounds, including the RAS–MAPK pathway and other signaling pathways, has been effective for ameliorating the defects in previous knockin mouse models of RASopathies. MEK inhibitors have been found to ameliorate the cardiac defects and skeletal features in mice expressing *SOS1* and *RAF1* mutations (24,35). Angiotensin II inhibitor ameliorates the phenotypes of hypertension, vascular remodeling and fibrosis of the kidney and heart in mice expressing *HRAS* G12V mutation (36), and mTOR inhibitor ameliorates hypertrophic cardiomyopathy in a mouse model of LEOPARD syndrome, expressing a catalytically inactive mutation in SHP2 (34). We examined a variety of compounds, including anti-cancer agents, MEK inhibitor, mTOR inhibitor, VEGFR3 inhibitor, BRAF inhibitor and farnesyl transferase inhibitor using our *Braf*$^{Q241R/+}$; *Cre* mice. Treatment with MEK inhibitor, but not mTOR inhibitor, in *Braf*$^{Q241R/+}$; *Cre* mice ameliorated embryonic lethality and skeletal abnormalities, suggesting that the pathogenesis of the disease is similar to those in *SOS1* and *RAF1* mutations. Thus, our new *Braf*$^{Q241R/+}$; *Cre* mice will be useful to screen various compounds for therapeutic approaches to RASopathies.

The exact mechanisms by which the single treatment of histone demethylase inhibitor or co-treatment of MEK inhibitor and histone demethylase inhibitor were effective for *Braf*$^{Q241R/+}$; *Cre* mice have not yet been characterized. Lysine modification of histone 3, acetylation and methylation, is associated with gene activation or silencing (37). In gene expression, inactive genes show methylation at lysine 27, and permanently silenced genes frequently are characterized by methylation at lysine 9 (37). Histone H3K27 methylase, *Ezh2*, conditional knockout mice in cardiomyocytes have been reported to show abnormal heart development, such as noncompaction and excessive trabeculation (38). Meanwhile, deletion of histone H3K27 demethylase, UTX, has been identified in individuals with Kabuki syndrome, who showed distinctive facial appearance and congenital heart disease (39). H3K9 methyltransferases, G9a and GLP, have been shown to be essential for cardiac morphogenesis (40). It is of note that the balance between methylation and demethylation of H3 is required for normal cardiac differentiation. *De novo* mutations in *SMAD2*, a transcription factor which regulates H3K27 methylation in embryonic left–right organizer, have been identified in children with congenital heart disease (28). *SMAD2*, which is regulated by ERK (41), has been found to bind to H3K27 demethylase JMJD3, and regulate H3K27 methylation

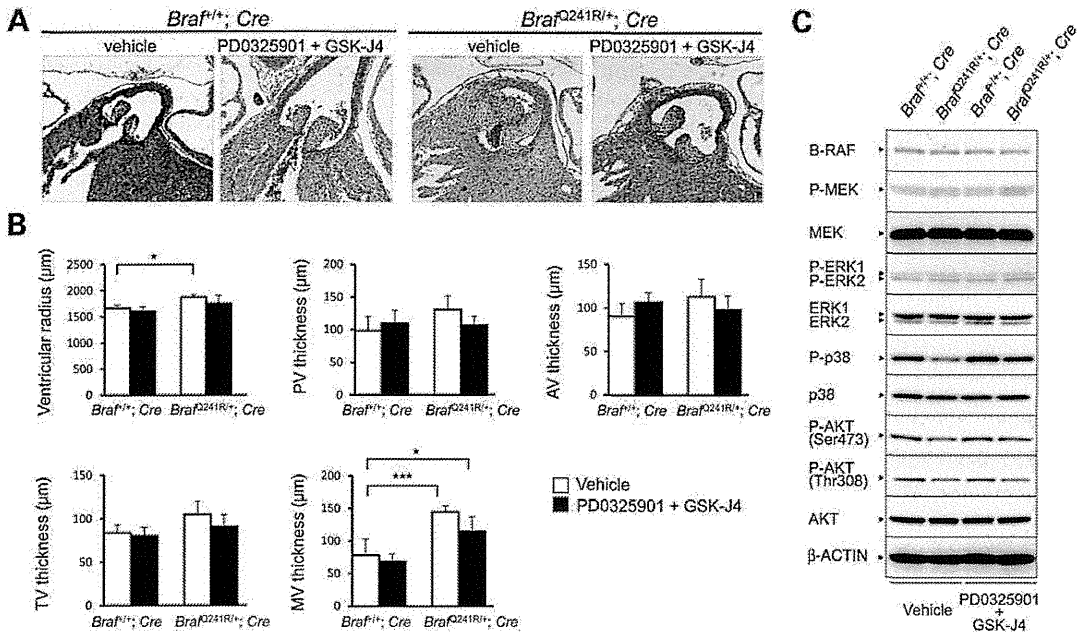

Figure 6. Influence of co-treatment with PD0325901 and GSK-J4 on the cardiac phenotype and signaling of *Braf*$^{Q241R/+}$; *Cre* embryos. (**A** and **B**) Sequential sections of embryonic hearts from *Braf*$^{+/+}$; *Cre* and *Braf*$^{Q241R/+}$; *Cre* at E16.5 stained H&E. (A) Histological sections of pulmonary valves. (B) The ventricular radius and the thicknesses of the cardiac valve leaflets were measured at their largest diameter in serial sections. Data are means ± SD (vehicle; *Braf*$^{+/+}$; *Cre* ($n = 5$), *Braf*$^{Q241R/+}$; *Cre* ($n = 5$). PD0325901 + GSK-J4; *Braf*$^{+/+}$; *Cre* ($n = 7$), *Braf*$^{Q241R/+}$; *Cre* ($n = 11$)). $^{*}P < 0.05$, $^{***}P < 0.001$ (Tukey–Kramer test). NS, not significant. (**C**) Western blotting of the hearts from *Braf*$^{+/+}$; *Cre* and *Braf*$^{Q241R/+}$; *Cre* embryos at E16.5 (vehicle-treated pooled samples; *Braf*$^{+/+}$; *Cre* ($n = 8$), *Braf*$^{Q241R/+}$; *Cre* ($n = 8$). PD0325901 + GSK-J4-treated pooled samples; *Braf*$^{+/+}$; *Cre* ($n = 8$), *Braf*$^{Q241R/+}$; *Cre* ($n = 7$)). β-Actin is shown as a loading control. The arrowheads indicate the bands corresponding to each protein.

(28), suggesting that the histone demethylase JMJD3 is associated with heart development in humans by indirect regulation of ERK. In addition, constitutively activated BRAF and RAS mutants, through ERK activation, have been shown to induce JMJD3 and EZH2 expression (42,43). These observations suggest that activation of BRAF or ERK is associated with histone H3K27 modification, regulating cardiac development. In this study, the total content of the H3K27me3 in heart tissues of *Braf*$^{Q241R/+}$; *Cre* or *Braf*$^{Q241R/+}$; *Cre* mice after GSK-J4 co-treatment with PD0325901 was comparable with that of *Braf*$^{+/+}$; *Cre* mice (data not shown). Furthermore, the histone H3K27 demethylase activity of lysates from *Braf*$^{Q241R/+}$; *Cre* embryos at E14.5 was comparable with that of *Braf*$^{+/+}$; *Cre* (data not shown). Further analysis of H3K9 and H3K27 modification status on individual genes will clarify the mechanism by which histone demethylase inhibitor is effective against embryonic and postnatal lethality and developmental defects in *Braf*$^{Q241R/+}$; *Cre* mice.

MEK inhibitor treatment or crossing with ERK1 knockout mice has improved the hypertrophy of cardiac valves in Noonan syndrome model mice with a *SOS1* or *PTPN11* mutation (24,44). In contrast, treatment of MEK inhibitor did not lead to the amelioration of enlarged cardiac valves in *Braf*$^{Q241R/+}$; *Cre* embryos. Furthermore, other mice, excluding *Braf*$^{Q241R/+}$; *Cre*, treated with MEK inhibitor showed enlarged cardiac valves (data not shown), suggesting that the vital nature of MEK/ERK signaling balance in cardiac valve development. Given that no MEK inhibitor activity nor the inhibition activity of other protein kinases has been reported in GSK-J1 (GSK-J4 sodium salt) (25), these results suggest that not only MEK/ERK signaling balance but also histone H3K27 modification can play a crucial role in the normal development of cardiac valve in *Braf*$^{Q241R/+}$; *Cre* embryos.

The natural history and the frequency of tumors in adult CFC patients have not been fully elucidated (6). Since molecular analysis became available, three individuals with *BRAF* mutation have been reported to have developed acute lymphoblastic leukemia and non-Hodgkin lymphoma (6). Knockin mice expressing *BRAF* L597V mutation survived to adulthood and showed multiple Noonan syndrome/CFC syndrome phenotypes, including short stature, facial dysmorphia and cardiac enlargement (12). The L597V is located in the CR3 kinase domain and leads to 2-fold elevated BRAF kinase activity (45). The L597V mutation has been identified in 11 somatic cancers (COSMIC; http://cancer.sanger.ac.uk/cancergenome/projects/cosmic/) and three patients with Noonan syndrome (13,46,47), which generally shows milder phenotype than that in CFC syndrome. In contrast, Q257R mutation is located in the CR1 domain and has been identified in 40% of CFC syndrome, not in cancers. Our ELK transactivation study has shown that level of ELK transactivation in Q257R was a half of V600E (3). The previous report showed that BRAF Q257R has increased BRAF kinase activity compared with WT and the activity was as high as that of the V600E (4). It is possible that differences in kinase activity and/or the effect on downstream pathways could cause the phenotypic differences in these knockin mice. Surviving *Braf*$^{Q241R/+}$; *Cre* mice in the PD0325901 treatment showed distinctive facial appearance, abnormal dental occlusion, reduced postnatal length and weight, kyphosis and skin

disease, which are similar to CFC syndrome phenotype (data not shown) (1,48). *Braf*$^{Q241R/+}$; *Cre* mice also survived to adulthood when these mice (C57BL/6J background) were crossed with ICR or BALB/c mice (unpublished data). Further studies will be necessary to examine if adult *Braf*$^{Q241R/+}$; *Cre* mice show phenotypes similar to patients with CFC syndrome, including seizures and tumor development.

The potential mechanism of activation and downregulation of multiple signaling pathways in *Braf*$^{Q241R/+}$; *Cre* embryos is unclear. In additional studies, we performed microarray analysis and quantitative real-time PCR using heart tissues from *Braf*$^{Q241R/+}$; *Cre* embryos at E13.5 or E16.5. Interestingly, mRNA levels of dual specificity phosphatase (*Dusp*) 2, 4 and 6, that inactivate ERK, p38 or JNK, and *Spry* 1, which inhibits the RAS–MAPK signaling pathway, were significantly higher in *Braf*$^{Q241R/+}$; *Cre* embryos than those in *Braf*$^{+/+}$; *Cre* (data not shown). In the present study, constitutive activation of phosphorylated ERK was not clearly observed in whole embryos and heart tissues from *Braf*$^{Q241R/+}$; *Cre.* These results suggest that increased mRNA levels of *Dusp* 2, 4, 6 and *Spry* 1 and decreased expression of phosphorylated p38 in embryonic heart could represent a negative feedback mechanism for normalizing constitutive ERK activation in *Braf*$^{Q241R/+}$; *Cre* embryos.

In summary, *Braf* Q241R-expressing mice provided an effective tool for studying the pathogenesis of CFC syndrome. It was found for the first time that combination treatment with PD0325901 and GSK-J4 is efficacious for the treatment of mice with the activation of the RAS–MAPK pathway. At present, clinical trials of a new MEK inhibitor, MEK162, are now being conducted to investigate the efficacy and safety of its use in Noonan syndrome with hypertrophic cardiomyopathy as well as in individuals with solid tumors, while no clinical trial of histone H3K27 demethylase inhibitor has been performed. Given that *BRAF* mutations cause cancer, combination therapy with MEK inhibitors and histone H3K27 demethylase inhibitors can be effective not only for the treatment of patients with RASopathies but also for the treatment of *BRAF* mutation-associated cancer in the future.

MATERIALS AND METHODS

Generation of *Braf*^{Q241R} knockin mice

To construct the targeting vector for *Braf*^{Q241R} knockin mice, a short arm containing *Braf* exon 5 and 6 (*Not*I-*Sac*II genomic DNA fragment), a long arm including exon 7, 8 (*Xma*I–*Bam*HI genomic DNA fragment) and the downstream of exon 8 (*Bam*HI–*Sac*I) were amplified using a Roswell Park Cancer Institute-23 BAC clone. The DNA fragments were ligated into the pBSIISK+ vector. The *Braf* Q241R (exon 7) mutation was introduced by site-directed mutagenesis. The *Psp*0MI–*Xho*I site was used to insert PGK-Neo-STOP cassette flanked by loxP sites. The targeting vector was linearized with *Sal*I and electroporated into ES cells (C57BL/6J background). To confirm correctly targeted ES clones, we performed genotyping, sequencing and the test of the Cre-mediated recombination system. Furthermore, homologous recombinants were confirmed by Southern blotting using 5′, 3′ and Neo probes. For this experiment, genomic DNA was digested with *Sac*I (5′ probe), *Nco*I (3′ probe) or *Afl*II (Neo probe). The probe sequences are shown in Supplementary Material, Table S5. Screened ES clones were then microinjected into BALB/c blastocytes and the resulting chimeras were crossed with C57BL/6J mice to obtain *Braf*$^{Q241R\ Neo/+}$ heterozygotes mice. Excisions of the PGK-Neo cassette and STOP codon were achieved by crossing of *Braf*$^{Q241R\ Neo/+}$ heterozygotes with CAG-Cre transgenic mice (*Braf*$^{+/+}$; *Cre*) on C57BL/6J background (RIKEN BioResource Center, Tsukuba, Japan; RBRC01828) (49). Animal experiments were approved by the Animal Care and Use Committee of Tohoku University.

Genotyping

Genomic DNA was prepared from tail tissue with DNeasy Blood & Tissue Kit (Qiagen, Hilden, Germany) or Maxwell 16 Mouse Tail DNA Purification Kit (Promega, Madison, WI, USA). Genotyping of the *Braf*$^{+/+}$, *Braf*$^{+/+}$; *Cre*, *Braf*$^{Q241R\ Neo/+}$ and *Braf*$^{Q241R/+}$; *Cre* was carried out by PCR using KOD FX Neo (TOYOBO, Osaka, Japan) or TaKaRa Taq (Takara Bio, Otsu, Japan) with the primers shown in Supplementary Material, Table S6.

Sequencing

Total RNA was extracted with TRIzol reagent (Invitrogen, Carlsland, CA, USA), and cDNA was synthesized using High-Capacity cDNA Reverse Transcription Kit (Applied Biosystems, Foster City, CA, USA). The exonic region in *Braf* was amplified by PCR using TaKaRa Taq with the primers including M13 sequences: 5′-GTAAAACGACGGCCAGTGAAGTACT GGAGAATGTCCC-3′ and 5′-AGGAAACAGCTATGACCC CACATGTTTGACAACGGAAACCC-3′. The PCR products were purified with QIAquick Gel Extraction Kit (Qiagen, Tokyo, Japan) and sequenced on an ABI 3500xl automated DNA sequencer (Applied Biosystems).

Quantitative reverse transcription–PCR

Quantitative PCR was performed using FastStart Universal Probe Master (ROX) (Applied Biosystems) with StepOnePlus (Applied Biosystems). Amplification primers and hydrolysis probes were designed using Universal ProbeLibrary Assay Design Center (https://qpcr.probefinder.com/roche3.html).

Alcian Blue/Alizarin Red staining

After embryos were placed in water for a day, the skin and viscera were removed. The eviscerated embryos were then fixed in 95% ethanol for at least 3 days and stained with 150 mg/l Alcian Blue 8GX (Sigma-Aldrich, St Louis, MO, USA), 80% ethanol and 20% acetic acid for 16–24 h. The stained embryos were rinsed with 95% ethanol and kept in 2% KOH for 16–24 h. They were then stained with 50 mg/l Alizarin Red (Sigma-Aldrich) and 1% KOH for 3 h, kept in 2% KOH for 12–48 h, placed in 20% glycerin/1% KOH for at least 5 days and stored in 50% glycerin.